The Determination of Transport Properties Using Dissipative Particle Dynamics: Investigation of Nanofluid Systems Involving Vapor-Liquid Equilibrium

THESIS

Presented in Partial Fulfillment of the Requirements for graduation with research distinction in Chemical Engineering in the undergraduate colleges of The Ohio State University

By

Nicholas T. Liesen

Undergraduate Program in Chemical and Biomolecular Engineering

The Ohio State University

2016

Thesis Committee:

Professor Isamu Kusaka, Advisor, Professor Lisa Hall

Abstract

In this work coarse-grained particle modeling and Monte Carlo simulation are used to investigate the physical and phase properties of a thin liquid film in equilibrium with a gas phase. The purely repulsive soft potential in Dissipative Particle Dynamics is replaced by the smoothing function from Smoothed Particle Hydrodynamics to accomplish this task. Transport properties of the liquid phase are determined by the application of Reverse Non-Equilibrium Molecular Dynamics within the framework of Dissipative Particle Dynamics and its energy conserving variation as developed by P. Español. The outcome of this work is used to investigate the possible role of thermally driven hydrodynamic instability in directing nanoparticle self-assembly.

Acknowledgments

Professor Isamu Kusaka

For the patience and guidance that he has extended to me over the course of the past year.

Professor Lisa Hall

For sacrificing her time to participate in my thesis defense.

The Office of Undergraduate Education & Undergraduate Research Office

For providing me with further encouragement to pursue this research work through the Research Scholar Award.

The Ohio Supercomputer Center

For supporting my simulations both in terms of computational time and technical support.

Wenda Williamson

For featuring my undergraduate research work within the Chemical Engineering department.

My Family

For their continued support.

Vita

2016.....B.S. Chemical Engineering, The Ohio State University

Fields of Study

Major Field: Chemical and Biomolecular Engineering

Table of Contents

List of Tables

List of Figures

Chapter 1: Introduction

§ 1.1: High Level Purpose

Nanoparticles (NP) have a diverse set of applications. In thermal management, nanofluids are employed to provide increased heat transfer without a corresponding increase in surface area. In nanomedicine, arrays of nanoparticles are utilized as the carriers for drug molecules. Many such applications, particularly those in nanomedicine and nanophotonics, rely on the ability to carefully manipulate the size and shape of the utilized nanomaterials (NM). One promising method to achieve the desired control is the bottom-up approach; NP and/or nanocluster (NC) building blocks and the weak and specific interactions between them (and the attached ligands) are used in order to assemble NMs. Despite the promise of this approach and the dependence of many applications on the degree of morphological control it is the case that current understanding of NM assembly is poor. As a result, there are not systematic procedures for bottom-up NM assembly. On a high level this work will contribute towards rectifying this issue. In order to accomplish this task an improved understanding of the behavior of systems in which these NMs assemble is necessary.

§1.2: Experimental Basis

The basis for this work is in experiments performed by Egusa. [5] [6] The system of interest is a thin layer of liquid which is heated from below, has a free upper surface, and contains sub-nanometer nanoclusters consisting of an inorganic core and attached

ligand molecules. The base fluid is binary and evaporates over time. Egusa demonstrated that, under certain conditions, this simple setup allows for precise control of NP shape and assembly. It is suggested that thermally-driven Bénard-Marangoni instability, which results from the surface tension gradient and leads to the formation of regular convection cells, is responsible for the observed NP self-assembly. Several observations suggest this hypothesis. Namely, that (1) the temperature dependence of the convection cell morphology corresponds exactly to that of the nanoparticle arrays and, (2) the NCs are observed to first to organize into an array of cells and then to form well-defined NPs.[12] The thought is that the formation of nanoparticles takes place inside the convection cells resulting from this instability. [12] In order to properly address the plausibility of the proposed mechanism of NP self-assembly it is necessary to determine transport coefficients. For the very complex fluid systems involved in Egusa's experiments, this requires that a number of difficulties be resolved which are of interest to researchers in the area of transport phenomena in nanoscale systems. Given the complexity of the system, determining the transport coefficients is not straightforward. Notably, neither the continuum description nor the molecular description is adequate; measures must be taken to address this difficulty.

§ 1.3: The Mesoscale Simulation Approach

Many systems cannot be appropriately addressed by an atomistic approach nor by a continuum approach. In order to deal with such systems mesoscale simulation approaches, such as dissipative particle dynamics, are frequently employed. The mesoscale lies somewhere between the two aforementioned approaches. There are many

reasons that one might want to utilize this approach. A few of these reasons are sketched out below.

(1) The system of interest has particular features which cannot be dealt with using continuum mechanical approaches. Examples include: contact lines, shocks, & interfacial regions. [4]

(2) In the situations characterized in (1) it is often the case that an atomistic approach, such as molecular dynamics, must be used in order to model these potentially crucial regions. Unfortunately, in most cases the size of the system of interest and/or the phenomena's time-span exceeds the available computational resources. Moreover, the level of detail captured in the molecular model is often unnecessary. In many cases it is, therefore, possible to capture the relevant details by appropriately course-graining the system.

(3) Often systems of interest involve many length scales. One such example is the simulation of the behavior of nanofluids. Mesoscopic approaches, and dissipative particle dynamics in particular, are well suited to tackle systems composed of multiple length scales.

(4) On very small length scales it is unclear that the continuum approach is applicable.

It is the same story as sketched out above with respect to the system of interest. The system has interfacial regions and features across multiple length scales due to the presence of nanoclusters, nanoparticles, and arrays of these nanoparticles in the base fluid. Moreover, many features of the system are on the nanometer scale. The scale of the

system taken together with the presence of the interfacial region and other complex features restrict us from applying the continuum approach. On the other hand attempting to capture these features by utilizing a molecular approach is prohibitively resource intensive. In order to cope with this difficulty many degrees of freedom (DOF) have been coarse-grained out and replaced at a stochastic level. Each of the 'dissipative particles' in the system represent a collection of atoms with internal DOF; this cuts down on necessary resources. The approach, referred to in the literature as dissipative particle dynamics (DPD), was introduced in 1992 by Hoogerbrugge and Koelman [11]. The original method was capable of reproducing correct hydrodynamic behavior in isothermal systems and consequently reproduced momentum transport. However, it lacked heat transport functionality. In order to allow DPD to study such systems DPDE, or DPD with energy conservation, was introduced simultaneously by (1) Español [8] and (2) Avalos & Mackie [2] into the literature. The energy conservation constraint is met by inclusion of an extra DOF (internal energy) for each particle. Consequently, a temperature and entropy can be associated with each particle. Moreover, particles can exchange energy stored in their internal DOF. Since both momentum and heat transport will be of interest DPDE will be employed. The system to which it is hoped that this approach can eventually be applied is sketched out in the section that follows.

§1.4: The System Of Interest

It is hoped that the methodology developed in this work can eventually be applied to a binary nanofluid mixture undergoing Bernard-Marngoni instability, a surface tension driven convective instability. The motivation for establishing this methodology is

a system where there is a thin film of liquid seated between a free surface and a plate. The plate is heated while the free surface is in contact with ambient air. As a result of this heating there are temperature fluctuations in the thin film of fluid at the interface with ambient air. As a result the lower temperature regions of the film surface (which have higher local surface tension) pull the higher temperature, lower local surface tension fluid towards its position. In order to preserve the interface the heated fluid flows upward toward the film surface. This hotter fluid reinforces the effect just described. It is the continual reinforcement of this behavior, driven by local surface tension gradients, which results in the development of a regime of regular convection cells. In general fluid is pulled up through the center of these cells, while the surface tension gradient pulls the fluid across and down the cell sides. Furthermore, there are certain conditions under which one can expect to observe the development of this pattern of convection cells. In particular, there are two dimensionless numbers which help to characterize the effect. The first is the Marangoni number; this number has a critical value above which one can expect to observe the effect. Stated more generally there is a point at which the forces due to differences in surface tension are sufficiently larger than the viscous forces for the instability to take place. Additionally, there is a Biot number; this number controls the critical value of the Marangoni number. As the Biot number increases the critical value of the Marangoni number increases. More generally, as the ratio of the internal conductive resistance to the external convective resistance increases, a higher ratio of thermal surface tension forces to viscous forces is required. The two dimensionless numbers are presented below. [12]

$$\mathrm{Ma} = \frac{|\frac{\mathrm{d}\sigma}{\mathrm{dT}}|\Delta \mathrm{T}\,\ell}{\eta\alpha} \propto \frac{Imbalance\ in\ \sigma\ due\ to\ inhomogeneity\ in\ T}{Viscous\ forces}$$

$$\mathrm{Bi} = \frac{\mathrm{h}\ell}{k} = \frac{Internal\ conductive\ resistance}{External\ convective\ resistance}$$

The system of interest in these simulations is very similar to that which is described above. The system consists of a thin layer of liquid – at the bottom of the liquid film a high temperature is imposed. The base fluid consists of a higher and lower boiling point solvent and has nanoclusters, nanoparticles, and arrays of these nanoparticles distributed in the fluid at various points in time. As evaporation of the base fluid proceeds the nanoparticles self-assemble in this gradually thinning layer of fluid. In order to properly address the plausibility of the proposed mechanism of NP self-assembly it is necessary to determine transport coefficients. The relevant transport coefficients which must be determined are listed below.

(1) $\eta: Viscosity\ of\ the\ Fluid$

(2) $k, \alpha: Thermal\ Conductivity\ \&\ Diffusivity$

(3) $h: The\ Heat\ Transport\ Coefficient\ at\ the\ vapor - air\ interface$

The temperature dependence of interfacial tension $|\frac{\mathrm{d}\sigma}{\mathrm{dT}}|$ must also be assessed. The evaluation of these properties and consequent determination of the value of these dimensionless numbers will allow the proposed mechanism of assembly to be more accurately accessed. As stated earlier the purpose of this work is to lay down the methodology for carrying out this work in the system of interest. In order to accomplish this task a simpler corresponding system is taken on. Rather than simulating a binary base

fluid with dispersed nanoclusters a simple single-component system is examined. The phase and transport properties along with the interfacial behavior is examined in this simpler system as a first step in evaluating the more complex system.

Chapter 2: Phase Behavior

§ 2.1: Simulation of VLE in DPDE

In order to determine transport properties in the system of interest DPDE, or Dissipative Particle Dynamics with Energy Conservation, as outlined earlier, is used. Dissipative particle dynamics is a course-grained simulation method which utilizes dissipative and random force components in order to control the temperature of the system; the friction or dissipative term cools down the system while the random or noise term heats the system up. The course-grained particles are imagined to have internal degrees of freedom and, therefore, internal energy. The dissipated mechanical energy due to the dissipative force is invested as heat in the internal degrees of freedom of the particles. Viscous heating and conductive effects are also taken into account when balancing the energy across the internal degrees of freedom of the particles. Conductive effects are taken into account via the exchange of internal energy between particles; exchanges occur due to equilibration and fluctuation when particles are sufficiently close to one another. A purely repulsive soft potential is used to determine the conservative interactions between particles.

$$\textit{Conservative}: \qquad \vec{F}_{ij}^{\,C} = \frac{-\partial U}{\partial |\vec{r}_{ij}|} = \alpha \omega_R(|\vec{r}_{ij}|)\vec{e}_{ij} \tag{1}$$

In (1) α controls the repulsive force strength. [17] A common choice of weighting function is the linear function presented below.

$$\omega_R = \begin{Bmatrix} 1 - \frac{r_{ij}}{r_c} \text{ for } r_{ij} \leq r_c \\ 0 \; otherwise \end{Bmatrix} \text{where } r_{ij} = |\vec{r}_{ij}| \tag{2}$$

The weighting function, $\omega_R = \omega_R(|\vec{r}_{ij}|)$, described above increases as the relative distance between the particles, $|\vec{r}_{ij}| = |\vec{r}_i - \vec{r}_j|$, decreases. This purely repulsive potential introduces difficulties for investigating the system of interest. Such a potential cannot reproduce vapor-liquid equilibrium behavior or phase change behavior. Moreover, after a thorough literature search it was determined that there were no published methods for simulating vapor-liquid equilibrium using DPDE. In order to simulate vapor-liquid equilibrium in DPDE a model proposed by Liu et al. [13] will be adopted and applied within the framework of DPDE. In this model a combination of polynomials serves as an interaction potential. One polynomial has a negative first derivative indicating a repulsive force. The second polynomial has a first derivative, $F = \frac{-d\phi}{dr}$, which is positive in sign indicating an attractive force. Together these polynomials form a potential which has both attractive and repulsive portions to it. Moreover, both the attractive and repulsive portions of the potential retain the softer interaction characteristic of clusters of molecules. This means that longer time steps can be taken in comparison to molecular dynamics. The result is that DPD retains its original advantages despite this modification. The form of the potential, as shown in Liu et al. is reproduced below.

$$U(|\vec{r}_{ij}|) = a[AW_1(|\vec{r}_{ij}|, r_{c1}) - BW_2(|\vec{r}_{ij}|, r_{c2})] \quad (3)$$

Where W_i is defined as indicated in (4).

$$W_i(|\vec{r}_{ij}|, r_{ci}) = \begin{cases} 1 - \frac{3}{2}\left(\frac{2|\vec{r}_{ij}|}{r_c}\right)^2 + \frac{3}{4}\left(\frac{2|\vec{r}_{ij}|}{r_c}\right)^3 & For\ 0 \leq \frac{2|\vec{r}_{ij}|}{r_{ci}} < 1 \\ \frac{1}{4}(2 - (\frac{2|\vec{r}_{ij}|}{r_c}))^3 & For\ 1 \leq \frac{2|\vec{r}_{ij}|}{r_{ci}} < 2 \\ 0 & For\ \frac{2|\vec{r}_{ij}|}{r_{ci}} \geq 2 \end{cases} \quad (4)$$

The conservative force is defined as in (5). A variety of potentials can be generated by

$$F_{ij}{}^{C} = -\frac{dU}{dr}\hat{e}_{ij} \quad (5)$$

modifying the cutoff radii (r_{c1}, r_{c2}), the interaction strength coefficient (a), and the magnitude of the attractive and repulsive portions of the potential which correspond to B and A respectively. The form of the potential is shown in Figure 1 for the case of a=18.5, B=1.0, A=2.0, r_{c1}=.8, and r_{c2}=1.0. It can be seen from the plot's slopes and Equation (5)

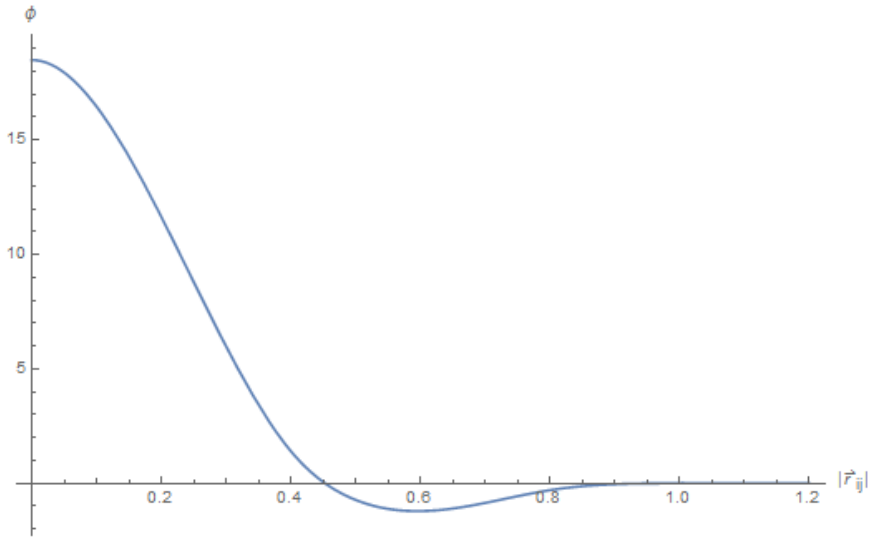

Figure 1: Cubic Spline Function, Potential

that there are attractive and repulsive portions of the potential. This observation is illustrated in Figure 2. Before implementing this potential with DPDE it was necessary

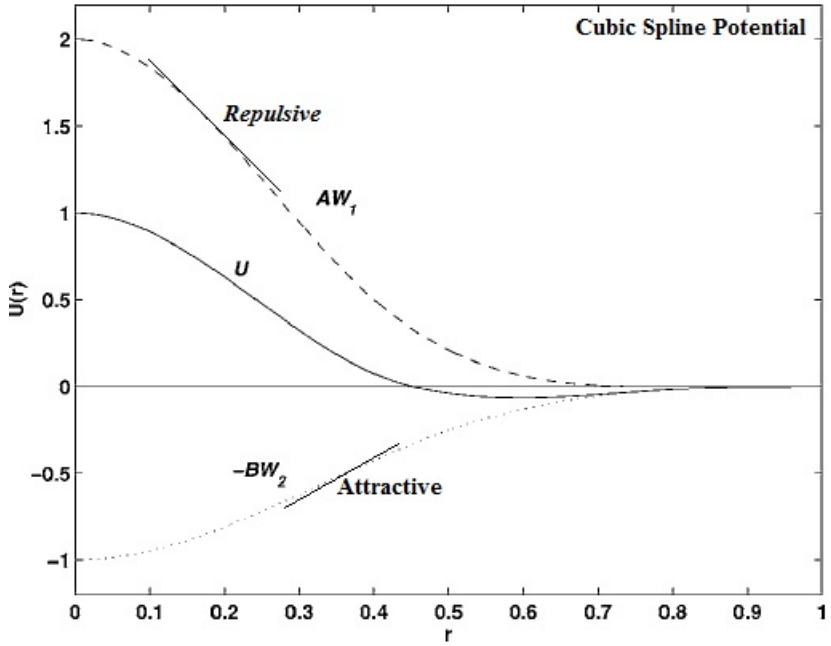

Figure 2: Liu Et al., Potential Illustration [13]

to determine the phase behavior of the system using this potential. This task, which includes the generation of phase envelopes and critical point temperatures was undertaken using A.Z. Panagiotopoulos' Gibbs' Ensemble Monte Carlo technique. [16]

§ 2.2: Phase Behavior; Gibbs Ensemble Monte Carlo

§§ 2.2.1: Introduction

Determination of the phase behavior of the system utilized the "Gibbs Ensemble" Monte Carlo (GEMC) technique. The GEMC technique is a computationally efficient way to model (vapor-liquid) phase coexistence. Typically, very large systems are necessary to simulate multi-phase behavior. This is because smaller systems are interface dominated. Additionally, long equilibration times make this approach resource intensive. In order to avoid these difficulties GEMC simulations make no attempt to simulate an interface. Instead, the liquid and vapor phases are modeled in separate but coupled simulation boxes. The experimental results in Figure 3 show particle positions in these simulation

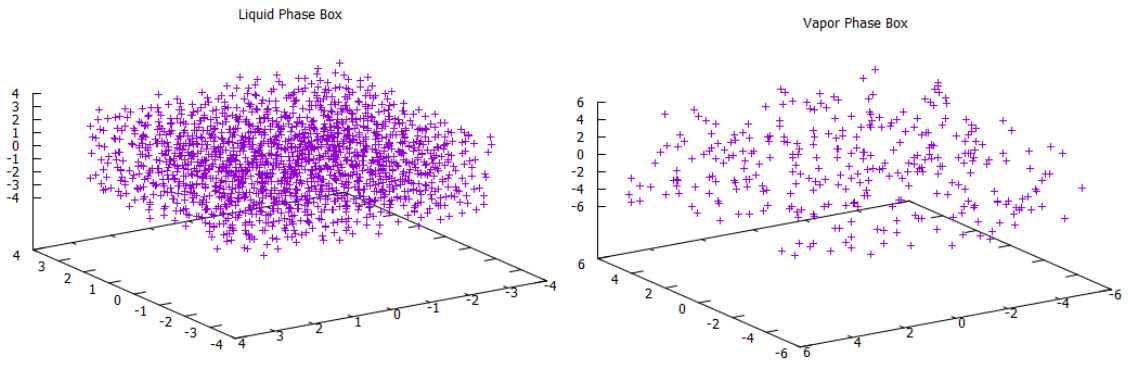

Figure 3: Gibbs Ensemble Simulation, Particle Positions

boxes. The simulation boxes exchange particles and volume and change particle locations. The simulations are performed isothermally while keeping total volume and number of particles fixed. Particles and volumes are exchanged in this manner in order to manipulate chemical potentials and pressures while treating the system, taken together, as

a canonical (N, V, T) ensemble. In fact, the Gibbs Ensemble can be shown to be rigorously equivalent to the canonical ensemble in the macroscopic limit, which has the normalized probability density function and configuration integral shown below. [10] The configuration integral is shown in Equation (8). Due to the fact that changes in the

$$\rho_{\mathrm{NVT}} = \frac{1}{Q_{\mathrm{NVT}}} \frac{1}{h^f N!} e^{-\beta(\mathcal{K}+\mathcal{U})} \tag{6}$$

$$where\ Q_{\mathrm{NVT}} = \frac{1}{h^f N!} \int e^{-\beta(\mathcal{K}+\mathcal{U})} \mathrm{dq}^f \mathrm{dp}^f \tag{7}$$

$$Z_{\mathrm{NVT}} = \int \mathrm{dr}^f e^{-\beta \mathcal{U}} \tag{8}$$

number of particles and volume are permitted in each individual simulation box, it is possible to make moves in such a way that the phase coexistence criteria ($\mu_I = \mu_{\mathrm{II}}, P_I = P_{\mathrm{II}}, T_1 = T_2$) is satisfied for the coupled simulation boxes. Figure 4 illustrates this principle. The configuration space was investigated using the potential introduced in the

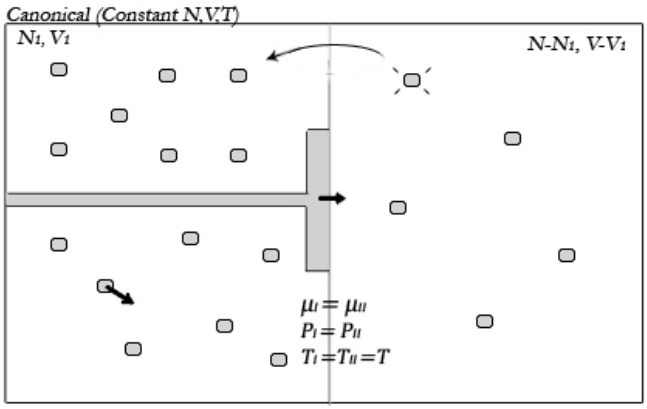

Figure 4: "Gibbs Ensemble" Monte Carlo Illustration[i]

previous section. Various configurations of particles are generated using the moves previously outlined. If the move results in a decrease of potential energy the move is accepted. This is done in order to push the particles in the direction of decreasing potential to a stable mechanical equilibrium. If the move results in an increase in potential energy the differences in potential, $\Delta\phi = \phi_f - \phi_i$, is calculated for the system using an appropriate cubic spline potential function. The probability that the move is accepted is proportional to, but not equal to, $e^{-\beta\Delta\phi}$. This follows from the fact that the limiting distribution is canonical. This technique was used to investigate the phase properties of a single component system. This investigation will serve as the basis for studying a binary mixture such as the system of interest outlined earlier.

§§ 2.2.2: Experimental Methodology

Gibbs ensemble Monte Carlo simulations were used to investigate the phase equilibrium of a single component system for various parameter choices within the interparticle potential. The coupled simulation boxes contained 2000 particles in total. Both simulation domains had periodic boundary conditions. The magnitude of the attractive portion of the potential, B, was varied while keeping the interaction strength coefficient, radii, and repulsive potential, $\phi_B = BW_2$, constant. Simulations were then performed at a series of different temperatures. Over the course of these simulations key system parameters such as internal energy per particle, pressure, and density were monitored for systematic drift to ensure that the behavior was that of a well-equilibrated system. The density, temperature, pressure and volume associated with each simulation box were then used to construct T-ρ and P-$\underline{V}$ phase envelopes and determine critical

points. Simulations could not be run too close to the critical point due to the formation of interfacial regions in both of the coupled simulation boxes. Then formation of an interface is favored under these conditions both entropically and in terms of free energy. As a result vapor-liquid coexistence cannot be observed close to the critical point. [10] For this reason the T-ρ phase envelopes were fit and the critical point was determined based on this fit.

§§ 2.2.2: Experimental Results

Various potential functions were used in the manner described in the experimental methodology. The magnitude of the attractive part of the potential was varied while

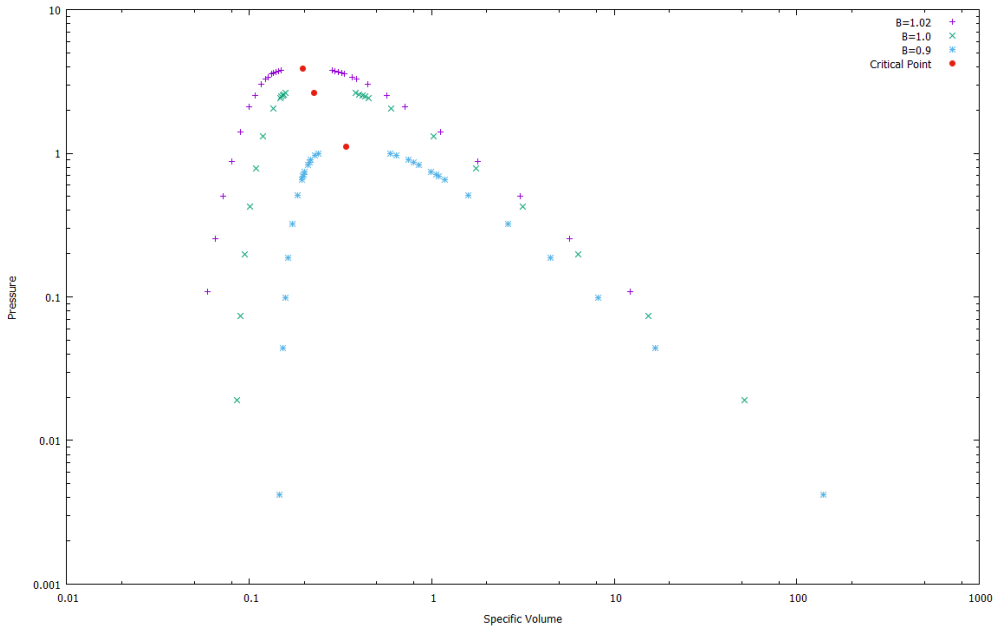

Figure 5: Pressure Vs. Specific Volume Phase Envelope

keeping the cutoff radii, overall interaction coefficient and magnitude of the repulsive portion of the coefficient constant. For the simulations detailed here a = 18.5 , A = 2.0, r-

r_{c1}=.8, and r_{c2}=1.0. B is varied from .9 to 1.02. This range of B-values allows for the investigation of a wide range of phase behavior. The resulting phase envelopes span a wide range of critical temperatures. The P-V and T-ρ phase envelopes are shown in Figure 5 and Figure 6 respectively. The densities are reported as $\rho^* = \rho_i {r_{c2}}^3$ where ρ_i is the number density in phase i. Temperatures are scaled using $k_B T$, divided by the energy parameter, ϵ. The energy scale is such that $\frac{\phi}{\epsilon} = 18.5(\phi_A + \phi_B)$ is the dimensionless potential where $\phi_A = \mathrm{AW}_1$ and $\phi_B = \mathrm{BW}_2$. potential where $\phi_A = \mathrm{AW}_1$ and $\phi_B = \mathrm{BW}_2$. Additionally, note that the unit of length corresponds to the cutoff radius of a single particle (1.0). Critical temperatures were determined by fitting the data to the law of

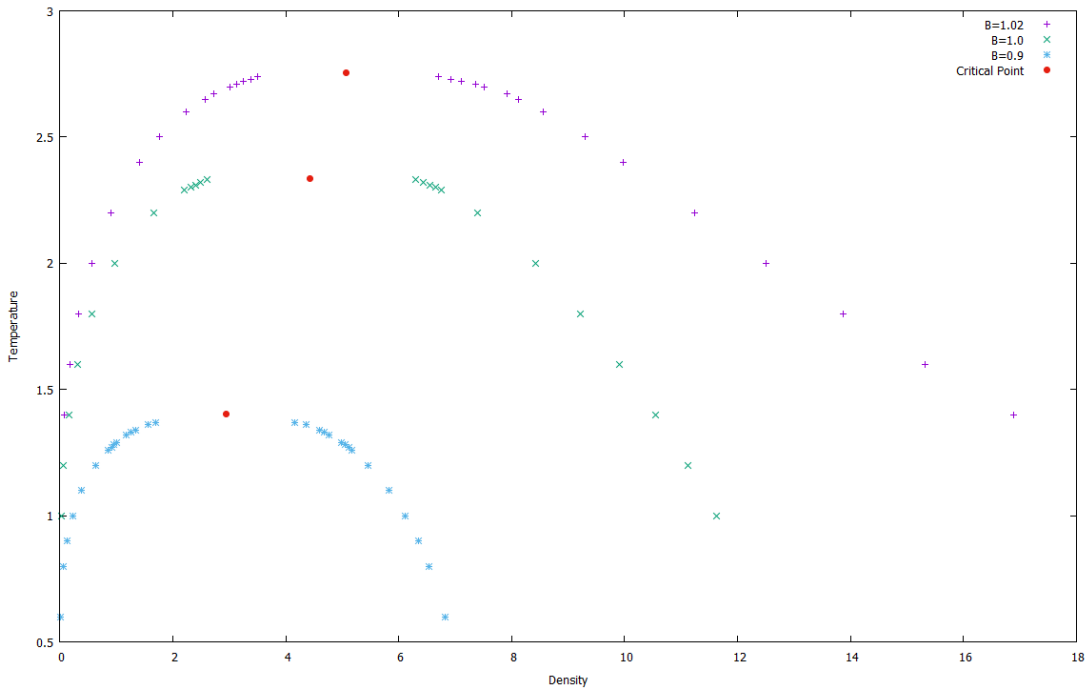

Figure 6: Temperature Vs. Density Phase Envelope

rectilinear diameters and a scaling law shown in Equations (9) and (10). [10] Here

$$\frac{\rho_l + \rho_v}{2} = \rho_c + \mathcal{A}(T - T_c) \tag{9}$$

$$\rho_l - \rho_v = \mathcal{B}(T - T_c)^{\beta} \tag{10}$$

$\mathcal{A}, \mathcal{B}$, and β are fitted parameters. The critical temperatures and pressures are listed below with their associated uncertainties. The value of β, the critical exponent, was .325.

Table 1: Critical Data

B-Value	Critical Temperature	Critical Pressure	Density
B=.9	1.4010	1.113	2.94
B=1.0	2.33379	2.627	4.430
B=1.02	2.756	3.892	5.07

Critical temperatures span a range of about 1.4 while pressures span a range of approximately 2.8. The fitted critical temperature and density data is shown for B=.9 in Figure 7. Reduced temperature versus reduced pressure and reduced density plots are

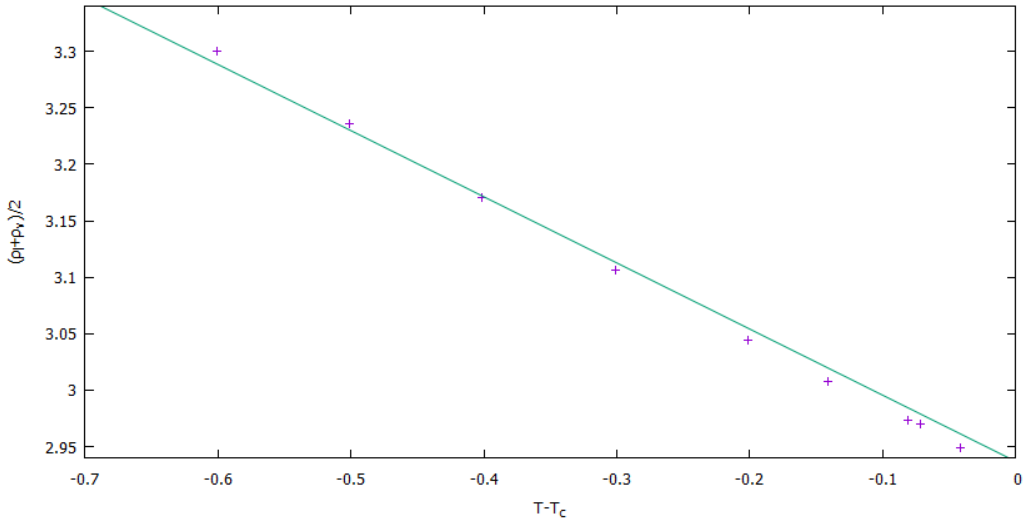

Figure 7: Fitted Data, Law of Rectilinear Diameters

shown in Figure 8 and Figure 9 respectively. It can be seen that the lines in these two plots are not isomorphic. This is consistent with expectations given that the model potential used is not a 2 parameter model.

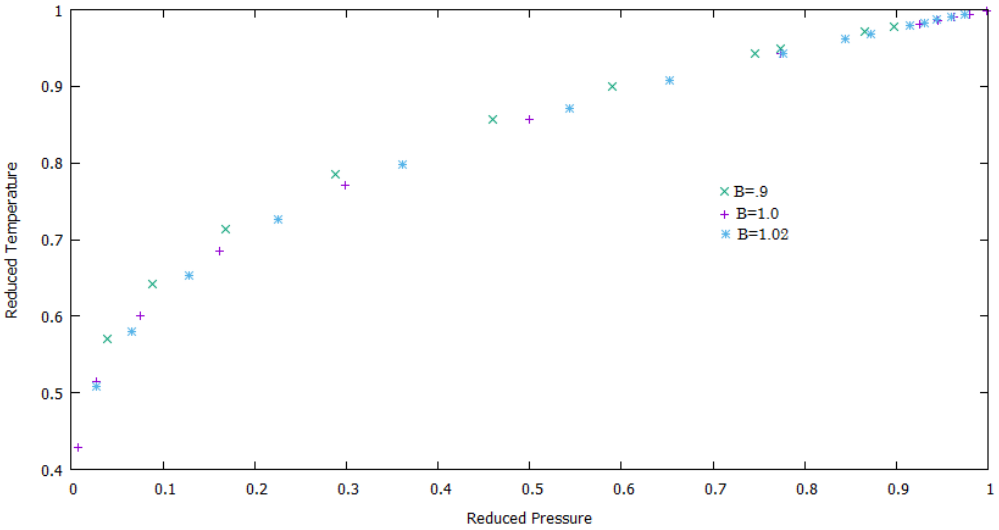

Figure 8: Reduced Temperature Vs. Reduced Pressure

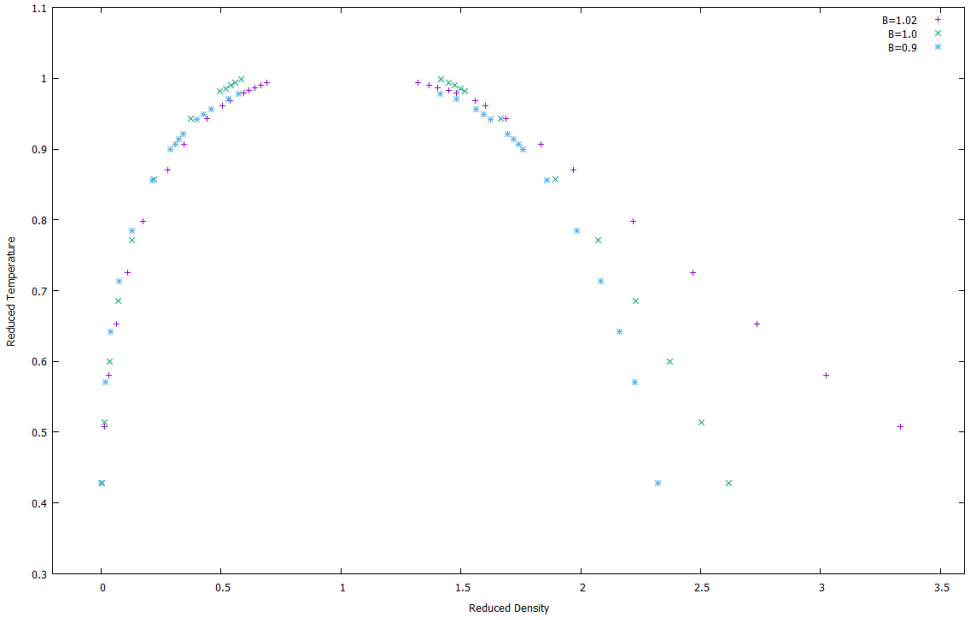

Figure 9: Reduced Temperature Vs. Reduced Density

Chapter 3: Interfacial Tension Simulations

§ 3.1: Introduction

The critical value of the Marangoni number, $\mathrm{Ma} = \frac{|\frac{\mathrm{d}\gamma}{\mathrm{dT}}|\Delta \mathrm{T}_l}{\eta\alpha}$, is a good indicator for the onset of Bernard-Marangoni instability. The Marangoni number depends on $|\frac{\mathrm{d}\gamma}{\mathrm{dT}}|$, the absolute value of the derivative of surface tension with respect to temperature. In order to determine the dependence of surface tension on temperature Monte Carlo simulations were performed. Similarly to the Gibbs Ensemble Monte Carlo simulations the configuration space was explored using the cubic spline function as a potential, as previously outlined. However, unlike the Gibbs Ensemble simulations the vapor and liquid phases are simulated in a single simulation domain. Moreover, unlike the Gibbs Ensemble simulations the interface is simulated.

§ 3.2: Experimental Methodology

Individual Simulations were performed using a constant box size, particle number, and temperature. As a result it is necessary that the limiting distribution used is canonical. In order to achieve this a particle is selected randomly and given some random but capped displacement. Energy of the configuration in the initial and final state, $\mathcal{U}_i$ and $\mathcal{U}_f$ are calculated. If $\mathcal{U}_f \leq \mathcal{U}_i$ then the move is accepted with probability one. If the move is not one which decreases the potential energy then the probability of accepting the move is proportional to $e^{-\beta\Delta\mathcal{U}} = e^{-\beta\Delta\phi}$. Simulations were performed over a wide range of temperatures in order to determine the dependence of surface tension on temperature. Additionally, as previously mentioned the vapor liquid and interface is all simulated

within a single simulation box. This simulation domain is shown in contrast to the coupled simulation boxes utilized in the Gibbs Ensemble simulations in Figure 10.

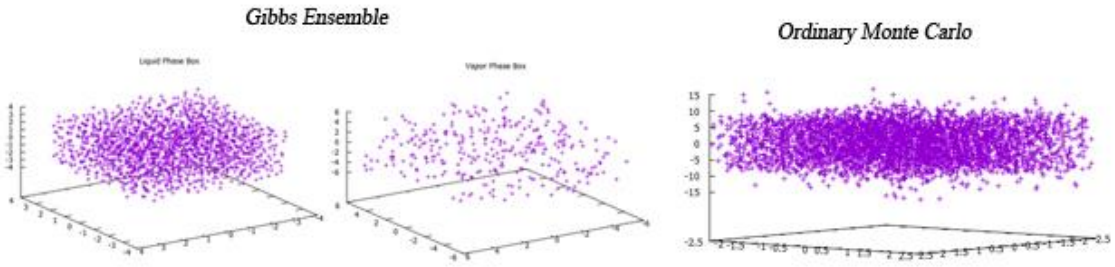

Figure 10: Gibbs Ensemble Vs. Ordinary Monte Carlo

Particles across the simulation domain were binned using bin lengths of .01 and density profiles were generated. The number of particles used was 4000. A box size of 60 x 5 x 5 = 750 was used for the B=.9 simulation set. A box size of 30 x 5 x 5 was used for all others. In order to determine the surface tension in this system the free energy for a constant N, V, T system is used. The free energy can be written as $F = F_v + F_L + F_i$ where F_i is the free energy of the interface and is equal to σA. Therefore, interfacial tension can be computed as shown in Equation (11). The thermodynamic free energy

$$\sigma = \left(\frac{\partial F}{\partial A}\right)_{N,V,T} \tag{11}$$

is related to the canonical partition function as shown in Equation (12).

$$F = -k_B T \ln(Q_{\mathrm{NVT}}) \tag{12}$$

Therefore, interfacial tension can be determined as below. As seen in the above

$$\sigma = -k_B T \frac{\partial \ln(Q_{\mathrm{NVT}})}{\partial A} = \frac{-k_B T}{Q_{\mathrm{NVT}}} \frac{\partial Q_{\mathrm{NVT}}}{\partial A} \tag{13}$$

development interfacial tension has physical units of energy per unit area.

§ 3.3: Experimental Results

As with the Gibbs ensemble simulations the methodology just described was applied using various forms of the cubic spline potential function. For the potential function $U(|\vec{r}_{ij}|) = 18.5[2W_1(|\vec{r}_{ij}|,.8) - .9W_2(|\vec{r}_{ij}|,1.0)]$ simulated at $\frac{k_B T}{\epsilon} = .8$ the particle distribution (I) and density profile (II) are shown in figure Figure 11. Similar figures are

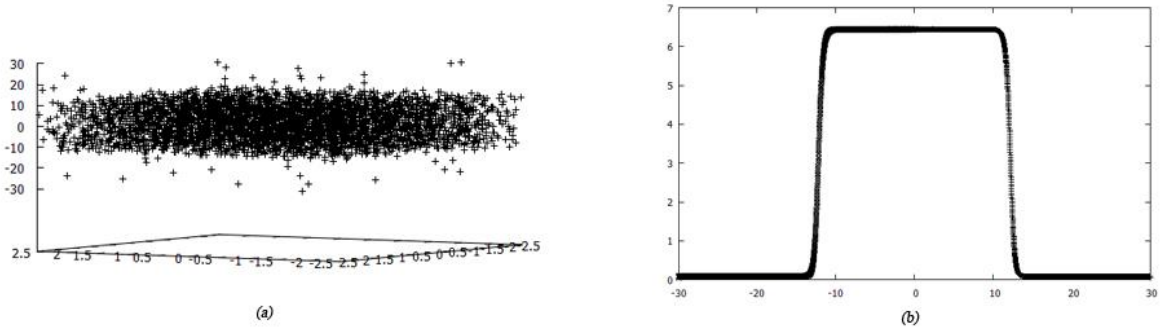

Figure 11: B=.9, T=.8 Particle Distribution (b) and Density Profile (a)

shown for scaled temperatures of .9, 1.0, 1.1, and 1.2 in Figure 12. The vapor density can be seen to increase with temperature while the bulk liquid density gradually decreases. The density profiles for all temperatures at which the simulation was run are shown superimposed on each other in Figure 13. For the potential function $U(|\vec{r}_{ij}|) = 18.5[2W_1(|\vec{r}_{ij}|,.8) - W_2(|\vec{r}_{ij}|,1.0)]$ simulated at $\frac{k_B T}{\epsilon} = 1.0$, 1.2, and 1.4 the particle

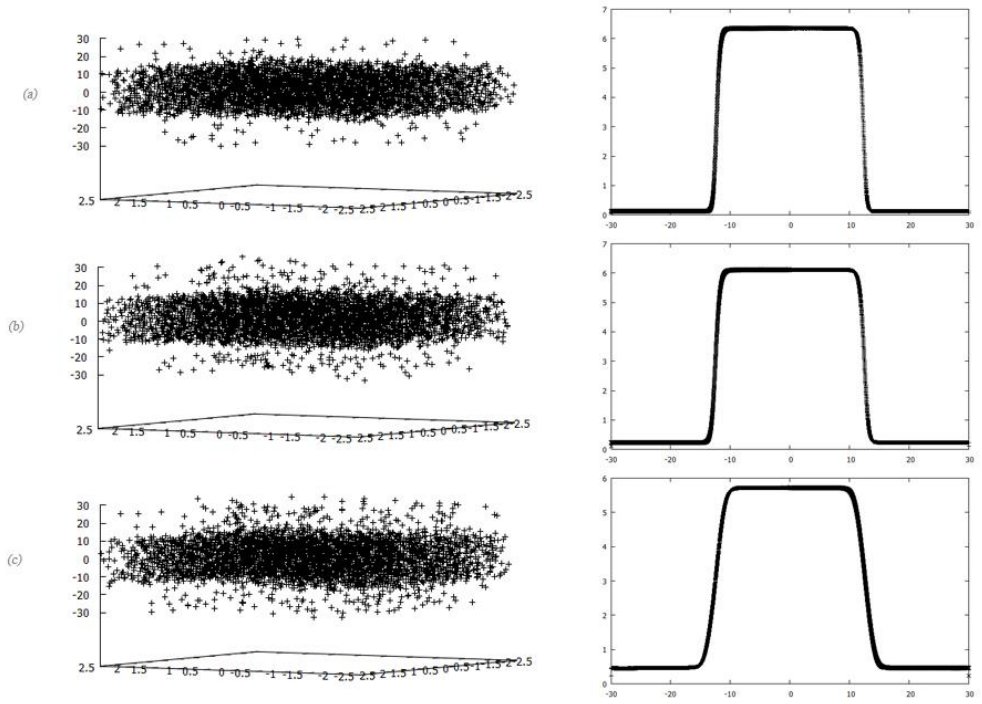

Figure 12: Particle Distribution and Density Profiles for (a) T=.9, (b) T=1.0 and (c) T=1.1

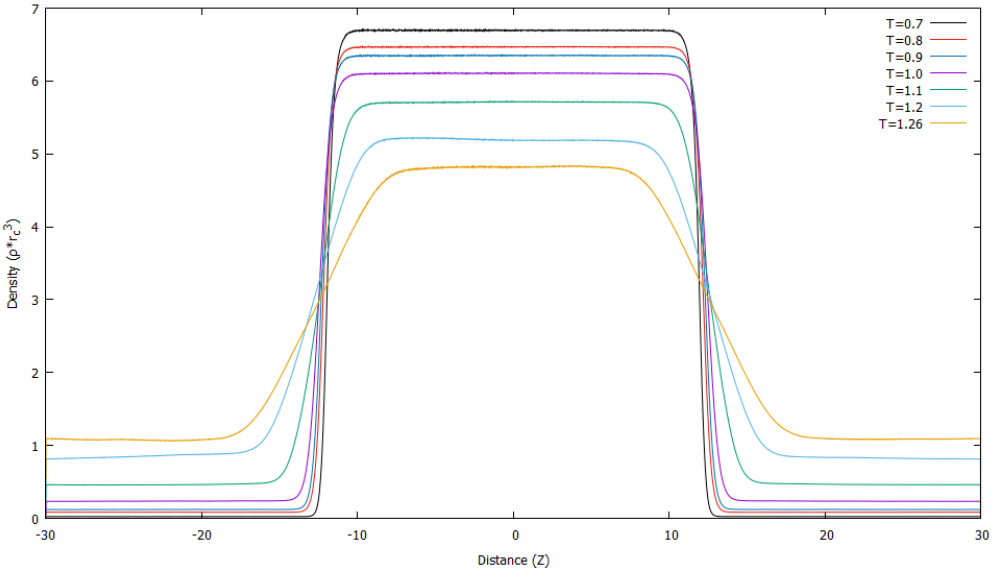

Figure 13: Density Profiles, B=.9

distribution functions and density profiles are shown in Figure 14. The resulting density

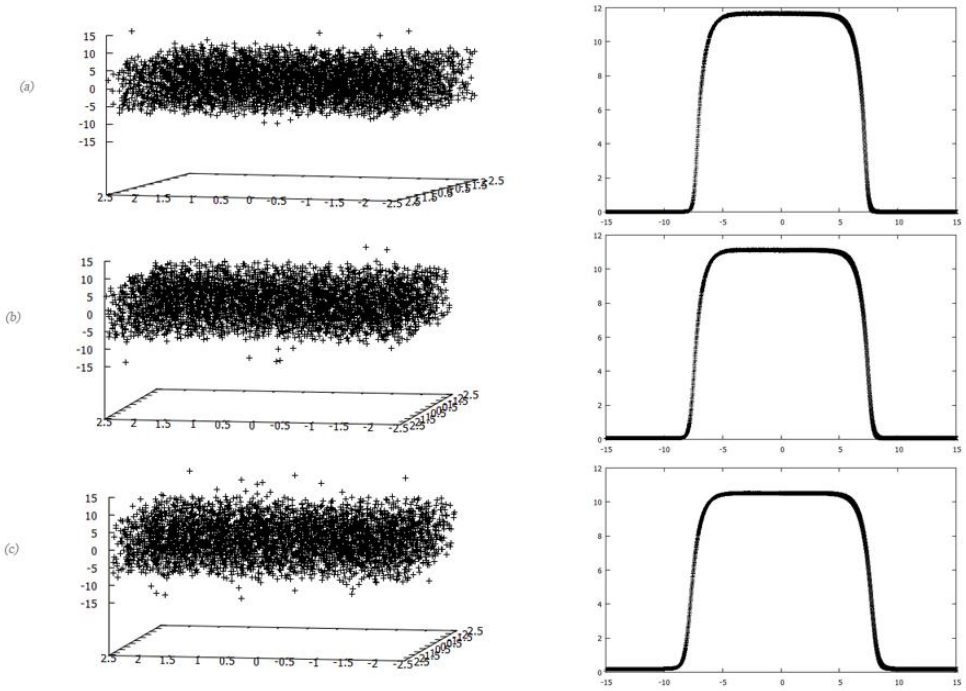

Figure 14: Particle Distribution and Density Profiles: T=1.0 (a), T=1.2 (b), T=1.4 (c)

profiles from all of the simulations are shown superimposed in Figure 15. Density

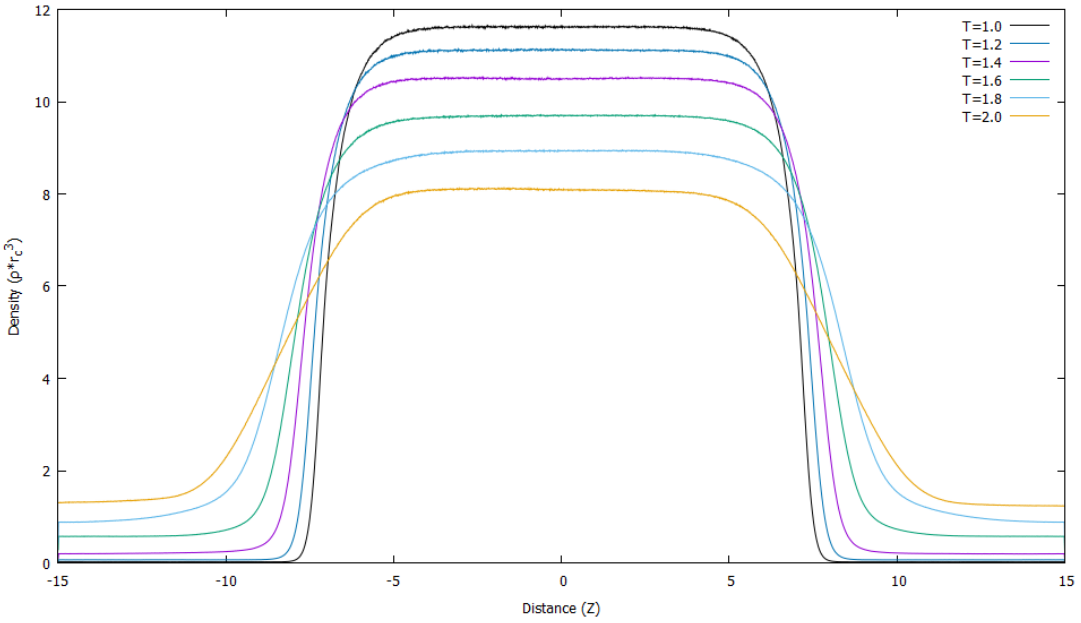

Figure 15: Density Profiles, B=1.0

profiles were also constructed for the potential function $U(|\vec{r}_{ij}|) = 18.5[2W_1(|\vec{r}_{ij}|, .8) - 1.02W_2(|\vec{r}_{ij}|, 1.0)]$. Particle distributions and density profiles are shown for select

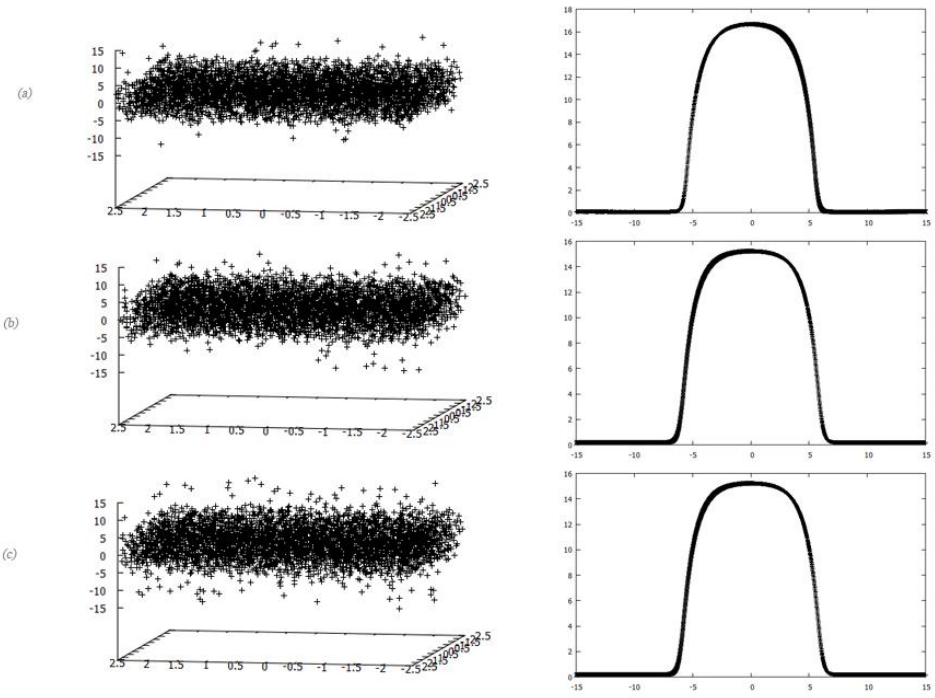

Figure 16: Particle Distribution and Density Profiles, T=1.4 (a), T=1.6 (b), T=1.8 (c)

temperatures in Figure 16. Density profiles for individual isothermal simulations with the attractive magnitude B=1.02 are shown superimposed in Figure 17. Density profiles for a B-value of 1.01 are shown in Figure 18. Interfacial tension values are reproduced in

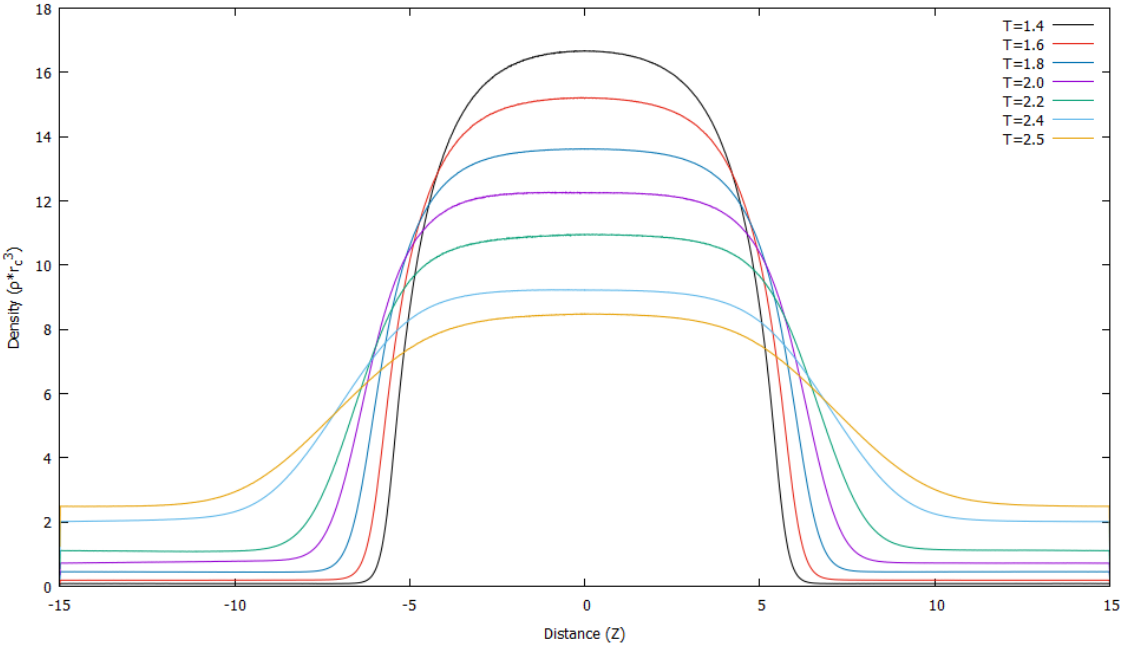

Figure 17: Density Profiles, B=1.02

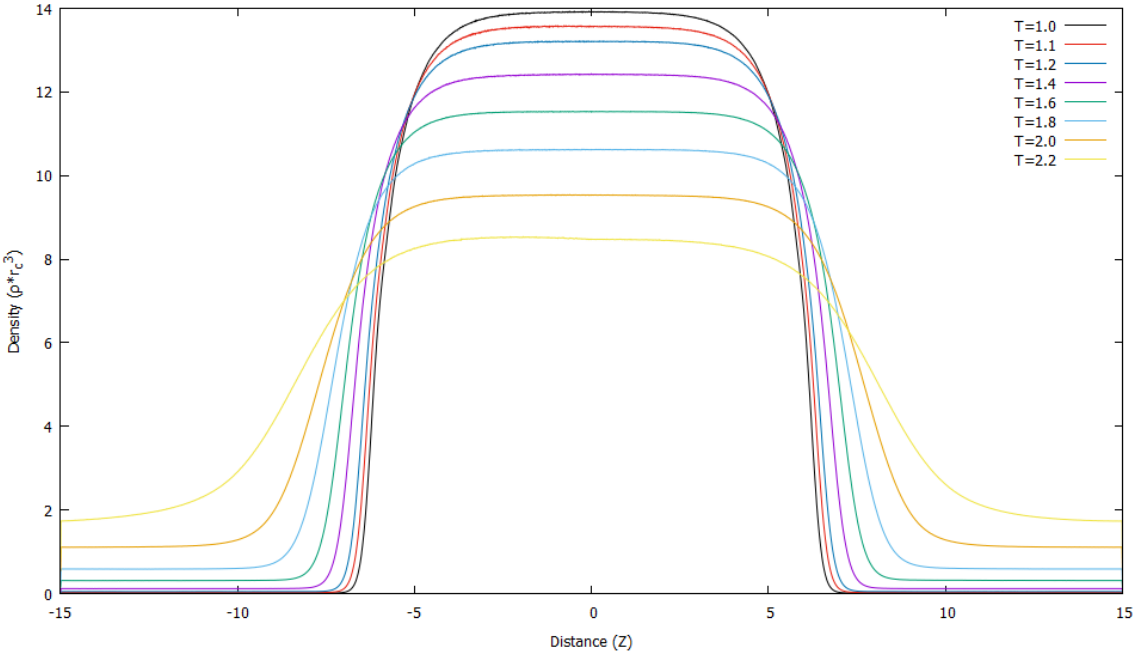

Figure 18: Density Profiles, B=1.01

Table 2 for B=1.0.Interfacial tension values are reproduced in Table 2 for B=1.0. As

Table 2: Interfacial Tension, B=1.0

T=1.0	7.59
T=1.2	6.44
T=1.4	5.24
T=1.6	4.02
T=1.8	2.86
T=2.0	1.71

expected interfacial tension decreases with the increase in temperature. Interfacial tension results for all B-values are represented in Figure 19.

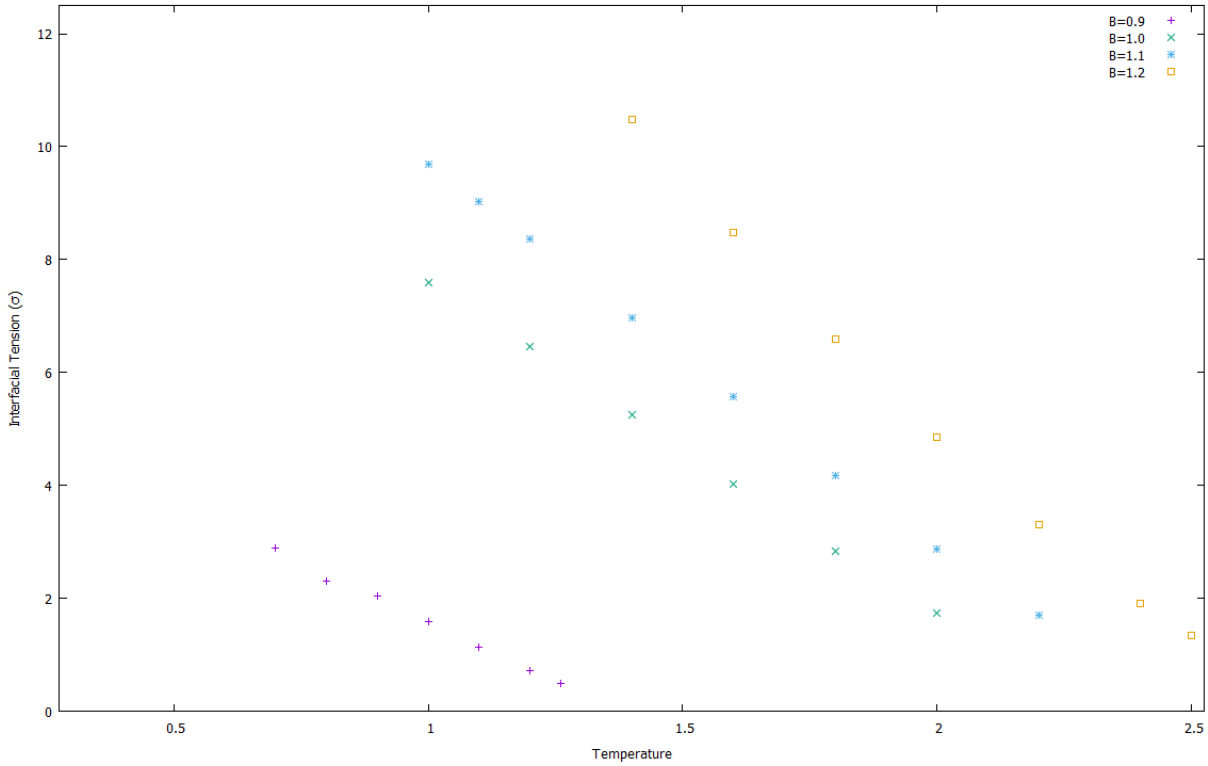

Figure 19: Interfacial Tension Vs. Temperature

Chapter 4: Isothermal Dissipative Particle Dynamics Simulations

§ 4.1: Introduction - Isothermal Dissipative Particle Dynamics

Dissipative particle dynamics is a coarse-grained simulation technique which utilizes dissipative, random, and conservative interactions to advance a systematically coarse-grained representation of a system through time. In isothermal dissipative particle dynamics the random and dissipative forces play a key role in keeping the system at a constant temperature. The equations of motion for the system are shown in Equations (14) and (15).[7] Equation (15) indicates that momentum is conserved.

$$\frac{d\vec{r}_i}{\mathrm{dt}} = \vec{v}_i = \frac{\vec{p}_i}{m_i} \tag{14}$$

As a result, the hydrodynamics of various systems can be reproduced. The accurate

$$\frac{d\vec{p}_i}{\mathrm{dt}} = m_i \frac{d\vec{v}_i}{\mathrm{dt}} = \sum_{j \neq i} \vec{F}_{\mathrm{ij}}^{\,C} + \vec{F}_{\mathrm{ij}}^{\,D} + \vec{F}_{\mathrm{ij}}^{\,R} \tag{15}$$

reproduction of the hydrodynamics is important in the determination of transport properties. The dissipative and random forces work together with two relationships derived from the fluctuation-dissipation theorem to function as a thermostat. The dissipative and random force expressions are shown in (16) and (17). [7]

Dissipative:
$$\vec{F}^{D}_{\mathrm{ij}} = -\gamma \omega_D(|\vec{r}_{\mathrm{ij}}|)(\vec{e}_{\mathrm{ij}} \cdot \vec{v}_{\mathrm{ij}})\vec{e}_{\mathrm{ij}} \tag{16}$$

Random:
$$\vec{F}^{R}_{\mathrm{ij}} = \sigma \omega_R(|\vec{r}_{\mathrm{ij}}|)\vec{e}_{\mathrm{ij}}\xi_{\mathrm{ij}} \tag{17}$$

Definition of the various terms is provided below [7]:

γ: The friction coefficient. This coefficient controls the rate at which the system is cooled down.

σ: Noise coefficient; this is a coefficient which controls the strength of the random kicks which heat the system up.

$\vec{r}_{\mathrm{ij}} = \vec{r}_{\mathrm{i}} - \vec{r}_{\mathrm{j}}$: This is the relative position term. That the force is dependent on relative velocity rather than absolute velocity is necessary in order to preserve Galilean Invariance.

$\vec{v}_{\mathrm{ij}} = \vec{v}_{\mathrm{i}} - \vec{v}_{\mathrm{j}}$: This is the relative velocity term. That the force is dependent on relative velocity is important in order to preserve Galilean invariance.

$(\vec{e}_{\mathrm{ij}} \cdot \vec{v}_{\mathrm{ij}})$: Español [7] notes that if the vector product of these factors in the dissipative term is positive it indicates that particle i is moving away from j and, therefore, feels a viscous force towards j. The inverse is also true.

ξ: Gaussian white noise variable. White noise is the time-derivative of Brownian motion, $\dot{W} = \xi$. [9] In practice ξ is generally taken to be a random variable. This reduces the required resources for the simulation.

The equations of motion can also be rewritten in terms of differential wiener elements as shown in Equations (18) and (19). Finally, the conservative force is generally taken as the

$$\frac{d\vec{r}_i}{\mathrm{dt}} = \vec{v}_i = \frac{\vec{p}_i}{\mathrm{m_i}} \tag{18}$$

$$d\vec{p}_i = (\sum_{j \neq i} F_{\mathrm{ij}}{}^{C}(|\vec{r}_{\mathrm{ij}}|) + \sum_{j \neq i} -\gamma\omega_D(|\vec{r}_{\mathrm{ij}}|)(\vec{e}_{\mathrm{ij}}.\vec{v}_{\mathrm{ij}})\vec{e}_{\mathrm{ij}})\mathrm{dt} + \sum_{j \neq i} \sigma\omega_R(|\vec{r}_{\mathrm{ij}}|)\vec{e}_{\mathrm{ij}}\mathrm{dW_{ij}} \tag{19}$$

derivative of a purely repulsive potential. The expression for the force is shown in

$$\vec{F}_{\mathrm{ij}}{}^{C} = \frac{-\partial U}{\partial \vec{r}_{\mathrm{ij}}} = \alpha\omega_R(|\vec{r}_{\mathrm{ij}}|)\vec{e}_{\mathrm{ij}} \tag{20}$$

Equation (20) where α controls the repulsive force strength. The weighting function

$$\omega_R = \begin{Bmatrix} 1 - \frac{r_{ij}}{r_c} \text{ for } r_{ij} \leq r_c \\ 0 \; otherwise \end{Bmatrix} \text{where } r_{ij} = |\vec{r}_{ij}| \tag{21}$$

is often taken to be the linear function presented in Equation (21). In the simulations run in this section a different potential is used. Rather than using this purely repulsive potential the cubic spline function potential from § 2.1: Simulation of VLE in DPDE is used. A Fokker-Planck expression can also be written which is equivalent to the momentum equation of motion previously introduced. This equation can be obtained using the fact that the average of a differential wiener element of order 1 is 0, the symmetry of the differential wiener element, a 'mnemotechnical Itō rule', $< dW_{ij}dW_{kl} >= (\delta_{ik}\delta_{jl} + \delta_{il}\delta_{jk})dt$, and the Chapman-Kolmogorov expression. The equivalent Fokker-Planck expression is shown in Equation (22) [7] where $x = \{x_1, x_2, \ldots x_N\}$ and $x_i = \{\vec{r}_i, \vec{v}_i\}$.

$$\frac{\partial \rho(x,t|x_o,t_o)}{\partial t} = L^{DR}\rho(x,t|x_o,t_o) - L^{C}{}_{\text{DPD}}\,\rho(x,t|x_o,t_o) \tag{22}$$

The Liouville operator for the system, $L^{C}{}_{\text{DPD}}$, written in terms of the conservative forces

$$L^{C}{}_{\text{DPD}} = \sum_i \vec{v}_i \frac{\partial}{\partial \vec{r}_i} - \sum_i \text{F}_i \frac{\partial}{\partial \vec{p}_i} \tag{23}$$

is shown in Equation (23) where $\text{F}_i = \sum_{j \neq i} \vec{F}_{ij}^{\,C}$. The operator corresponding to the

$$L^{DR} = \sum_i \sum_{j \neq i} \vec{e}_{ij} \frac{\partial}{\partial \vec{p}_i} [\gamma \omega_D(|\vec{r}_{ij}|)(\vec{e}_{ij}.\vec{v}_{ij}) + \frac{\sigma^2}{2}(\omega_R(|\vec{r}_{ij}|))^2 (\frac{\partial}{\partial \vec{p}_i} - \frac{\partial}{\partial \vec{p}_j})] \tag{24}$$

thermostatting forces is shown in Equation (24).[7] The final thermostat relation can be obtained by assuming a reasonable form for ρ_{eq} and examining the conditions under which the Fokker-Planck expression corresponds to an equilibrium solution

($\frac{\partial \rho}{\partial t} = 0$). One way to accomplish this task is to set (A) $L^{C}{}_{\mathrm{DPD}}\rho_{\mathrm{eq}} = 0$ and (B) $L^{DR}\rho_{\mathrm{eq}} = 0$. Assuming that the equilibrium statistical weight expression,

$$\rho_{\mathrm{eq}} = \frac{1}{Z} e^{-\beta \mathrm{H}} \text{ where } H = \sum_{i} \frac{{p_i}^2}{2m_i} + V(r) \quad (Canonical\ Ensemble) \tag{25}$$

ρ_{eq}, corresponds to that of a canonical (Constant N,V,T) ensemble, Equation (25), it is discovered that the following two conditions are sufficient to satisfy (A) and (B).

$$\omega_D{}^{1/2} = \omega_R \text{ and;} \tag{26}$$

$$\sigma^2 = 2k_B \mathrm{T}\gamma \tag{27}$$

Condition (27) taken together with the dissipative and random forces constitutes the thermostat of the system. The temperature of the system is fixed together with either the noise or friction coefficient.[ii]

§ 4.2: Introduction - Reverse Non-Equilibrium Molecular Dynamics, Viscosity

In 1872 James Clerk Maxwell presented a thought experiment, now referred to as "Maxwell's Demon", in his book *Theory of Heat*. The thought experiment describes a demon who monitors the kinetic energy of all the particles in a system. The gas is partitioned into two sides by a wall with a moveable, frictionless partition. One side of the wall contains gas with a lower average kinetic energy than the other side. The demon opens the partition whenever a high kinetic energy molecule on the cooler side will pass through to the hotter side or a molecule on the hotter side with low kinetic energy will pass to the cooler side. The end result of this is that heat will transfer from a cooler body to a hotter one in violation of the second law of thermodynamics. This thought experiment was the subject of much debate. This idea of a Maxwellian demon which can pick out molecules with particular properties and manipulate them is utilized in the

method of Reverse Non-Equilibrium Molecular Dynamics (RNEMD). The simulation domain is split into bins of a particular width along the z-direction. In order to establish steady-state shear flow the particles in the central bin are driven in, say, the positive x-direction and the particles in the bin on the bottom are driven in the negative x-direction. Using a demon to perturb the edges of the profile accomplishes this task. Particles with the most negative p_x component in the bin desired to move in the +x direction have the x-component of their momentum values swapped with particles in the –x bin moving with the most positive positive p_x component. In order to conserve linear momentum and kinetic energy it is important that $m_1 = m_2$. This principle is illustrated in Figure 20. If this swap is performed under steady-state conditions "the momentum will flow back

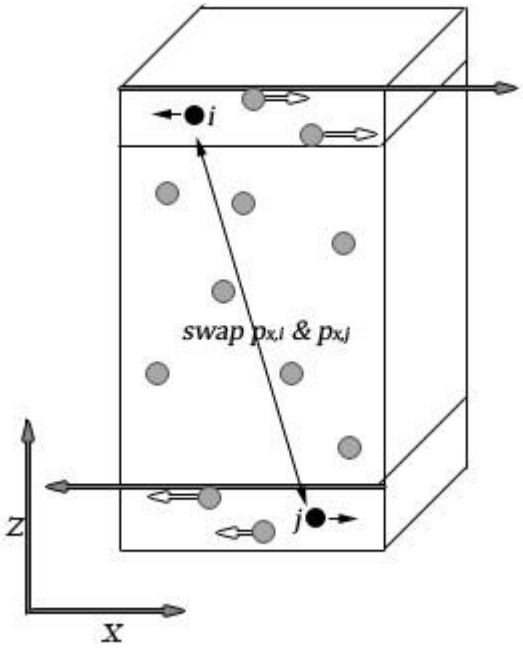

Figure 20: RNEMD, Principle Illustration - Viscosity

through the fluid by friction". In fact, in steady-state the momentum transferred by these swaps will be equal to the "momentum flowing back through the fluid by friction". [15] This equilibrium behavior results in a constant shear rate regime across the fluid. The only exception is the outside edges of the velocity profile which have been perturbed by the swapping. The momentum transferred in each of these swaps can be calculated very conveniently as $\Delta P_{x,s} = mv_{x_1} - mv_{x_2}$. Thus, the total momentum can be calculated as a sum over all swaps, $\sum_S \Delta P_{x,S}$. Average momentum flux can then be calculated according

$$< \tau_{zx} >= \frac{\sum_S \Delta P_{x,S}}{2t \cdot A} \tag{28}$$

to Equation (28) where t is the time of the simulation and A is the cross sectional area. [15] The average velocity values are then calculated according to Equation (29) in each

$$< v_x > = \sum_i v_{x,i} \tag{29}$$

of the bins where i is an index over the number of particles in the bin. Shear rate, $\dot{\gamma} = \frac{dV_x}{dz}$, is then calculated as the slope of the velocity profile. The viscosity can then be recovered from this shear flow using Newton's law of viscosity, Equation (30).

$$\tau_{zx} = \eta\dot{\gamma} \tag{30}$$

§ 4.3: Methodology – Viscosity Computation

During the Monte Carlo portion of this work phase envelopes and density profiles for a single component system utilizing a cubic spline function potential as laid out in Liu et al. were determined. The goal of this section of the work was to determine viscosity in the bulk liquid phase of the single-component system previously studied using Monte Carlo.

This was accomplished by using the bulk liquid phase density obtained during the Monte Carlo simulations and calculating the correct number of particles for a box of size of 5x5x10. The relaxation & equilibration of the system was carried out by first relaxing the configuration of the particles. Once the configuration was sufficiently relaxed the particles were assigned velocities according to a Maxwell distribution. The simulations to recover viscosity and actual equilibration of the system were carried out using isothermal dissipative particle dynamics (DPD). The conservative force was determined using the cubic spline function previously mentioned. In order to determine the viscosity the method of RNEMD outlined in § 4.2: Introduction - Reverse Non-Equilibrium Molecular Dynamics, Viscosity is applied within the framework of DPD. Using this method viscosity is recovered from the shear flow induced in the system. Simulations at many different bulk liquid densities along the phase envelope are performed using a single noise coefficient, σ . These simulations are performed using cubic spline potential functions with varying magnitudes of the attractive potential, B. Additionally, at a single temperature simulations are performed where the value of the noise coefficient is varied. In each of these simulations the shear stress or momentum flux is calculated using the method outlined in § 4.2: Introduction - Reverse Non-Equilibrium Molecular Dynamics, Viscosity and the shear rate is calculated from the velocity profile (V_x vs. Z). When determining this slope the perturbed edges of the velocity profile are not used. As outlined earlier, this shear rate should be constant across the profile. Viscosity is then calculated using the obtained momentum flux from the swaps and the shear rate from the velocity profile.

§ 4.4: Isothermal DPD - Experimental Results

All simulations in this section were performed using a simulation box of size 5x5x10 with periodic boundary conditions. The number of particles were calculated using the densities obtained in the Monte Carlo simulations. A table is provided below indicating

	B=.9	B=1.0	B=1.01	B=1.02
T=.8	1635			
T=.9	1587			
T=1.0	1529	2908	3482	
T=1.1	1457		3395	
T=1.2	1365	2794	3303	
T=1.26	1292			
T=1.4		2635	3109	4224
T=1.6		2477	2906	3832
T=1.8		2303	2696	3466
T=2.0		2104	2477	3128
T=2.2				2809
T=2.4				2494

The number of particles used in any given simulation for the dimensionless potential function $\frac{\phi}{\epsilon} = 18.5(\phi_A + \phi_B)$ where $\phi_A = \mathrm{AW}_1$ and $\phi_B = \mathrm{BW}_2$. A linear weighting function was used for the repulsive weighting function. The mapping of positions and velocities from one step to the next, $\mathcal{S}_{\Delta t}[\vec{r}(t), \vec{v}(t)] = (\vec{r}(t + \Delta t), \vec{v}(t + \Delta t))$, is accomplished through the use of a (1st order) Trotter decomposition, $\mathcal{S}_{\Delta t} = \mathcal{S}_{\Delta t}{}^{C}\mathcal{S}_{\Delta t}{}^{S}$ where $\mathcal{S}_{\Delta t}{}^{C}$ is the conservative propagator and $\mathcal{S}_{\Delta t}{}^{S}$ is the stochastic propagator. The time steps taken, Δt, have length .001. The swap frequency was taken to be 10 exchanges every 1000 time steps. The simulation domain is split into bins of width .2 along the z-axis for the purpose of performing momentum swaps. The total length from the end of the central box to the start of the box at Z=0 is 5.0. For the simulations investigating the varying of the noise coefficient a temperature $\frac{k_B T}{\epsilon}$ of 1.0 is selected. The

value of the noise coefficient is varied in the range of 1 to 10. The shear rate can be seen to decrease with increasing values of σ in Figure 21. Additionally, the viscosity can be seen to increase with increasing values of the noise coefficient in Table 3. This result is to be expected. As the noise coefficient, σ, increases the friction coefficient increases by the relation $\gamma = \frac{\sigma^2}{2k_B\mathrm{T}}$ which is a rearrangement of (27). The increase in the friction coefficient results in an increase in magnitude in the viscous force, $\vec{F}^D{}_{\mathrm{ij}}$, which, to some extent, represents the effect of viscosity making it more difficult for particles to move with respect to one another. Additionally, for an attractive potential

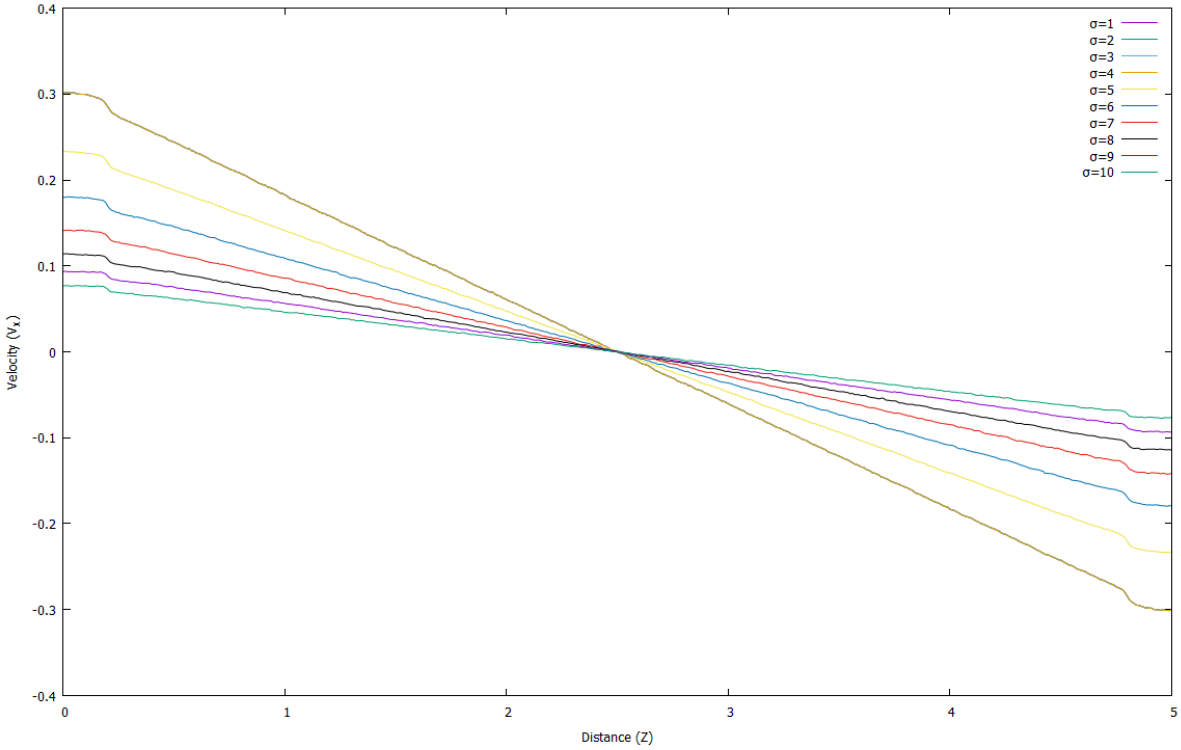

Figure 21: Velocity Profiles, Varying Noise Coefficient

magnitude of B=1.0 results are reproduced below for various temperatures along the

Table 3: Viscosity, Varying Noise Coefficient

Noise Coefficient, σ	Viscosity, η
1	3.1914
2	3.9603
3	5.327
4	7.308
5	9.787
6	12.960
7	16.841
8	21.21
9	26.28
10	31.96

phase envelope. Figure 22 shows the velocity profiles for the various temperature simulations. Shear rate can be seen to increase with temperature. Table 4 shows the

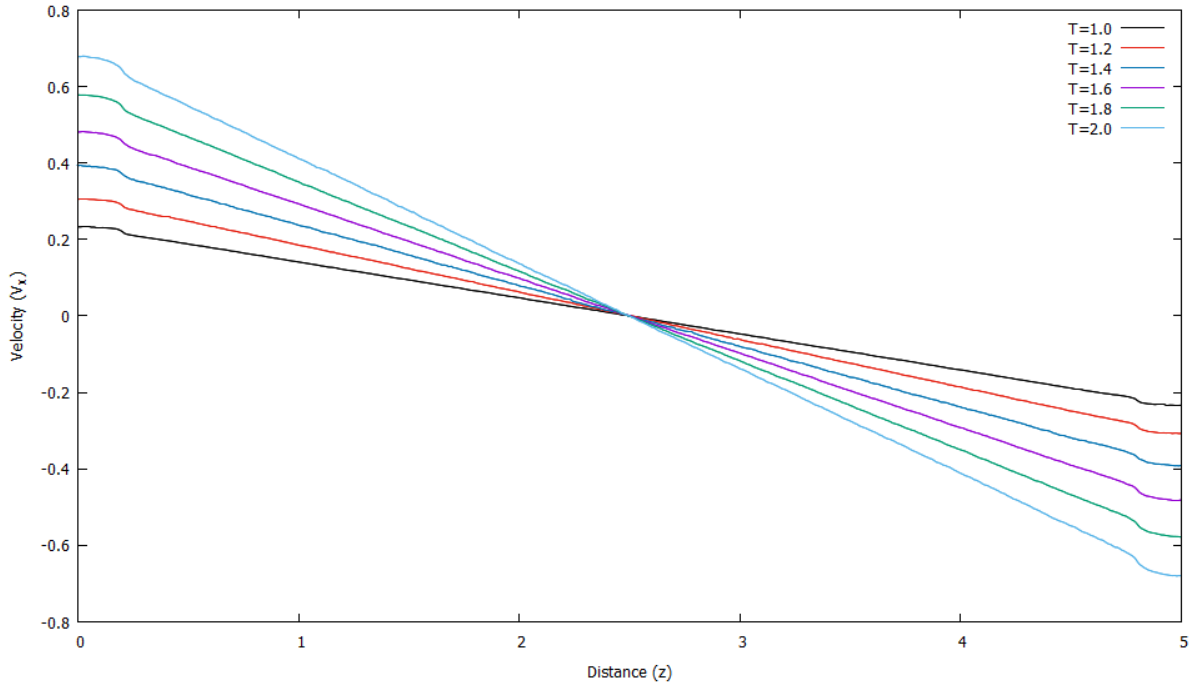

Figure 22: Velocity Profiles, B=1.0

values of viscosity determined over the course of these simulations. The results are

Table 4: Viscosity Vs. Temperature, B=1.0

Temperature	Viscosity, η
1.0	9.790
1.2	6.058
1.4	4.737
1.6	3.8522
1.8	3.2127
2.0	2.7351

consistent with the temperature dependence of viscosity. As temperature increases viscosity decreases.

Chapter 5: Dissipative Particle Dynamics with Energy Conservation Simulations

§ 5.1: Introduction - DPDE

Dissipative particle dynamics was introduced simultaneously in the literature by (1) Pep Espanol [8] and (2) Avalos & Mackie. [3][14] The formulation introduced in this section follows the development by Espanol. In dissipative particle dynamics with energy conservation (DPDE) the coarse-grained particles are imagined to have internal degrees of freedom and, therefore, internal energy. DPDE uses the same dissipative and random forces as DPD however, dissipated mechanical energy due to the former force is invested as heat in the internal energy of the particles while the random forces are withdrawn from the internal energy. Additionally, the internal energy of these particles is subject to heat conduction and thermal fluctuation behaviors provided distance between the particles is

appropriate. Energy is conserved with in this system meaning the total mechanical energy plus internal energy equals a constant value, as indicated in Equation (31). [8] The

$$\frac{\mathrm{dE_{mec}}}{\mathrm{dt}} + \sum_{\mathrm{i}} \frac{\mathrm{d}\epsilon_{\mathrm{i}}}{\mathrm{dt}} = 0. \tag{31}$$

equations of motion within DPDE for position, momentum, and internal energy are introduced in Equations (32), (33), and (34) below. [1][iii] The equation of state is also introduced in Equation (35). Here the dissipative, random, and conservative forces are the

Position
$$\frac{d\vec{r}_i}{\mathrm{dt}} = \vec{v}_i = \frac{\vec{p}_i}{m_i} \tag{32}$$

Momentum
$$m_i \frac{d\vec{v}_i}{\mathrm{dt}} = \frac{d\vec{\rho}_i}{\mathrm{dt}} = \sum_{j \neq i} (\vec{F}_{\mathrm{ij}}^{\,C} + \vec{F}_{\mathrm{ij}}^{\,D} + \vec{F}_{\mathrm{ij}}^{\,R}) \tag{33}$$

Internal Energy
$$\frac{\mathrm{d}\epsilon_i}{dt} = C_V \frac{\mathrm{dT}_i}{\mathrm{dt}} = \sum_{j \neq i} (q_{\mathrm{ij}}{}^{\mathrm{cond}} + q_{\mathrm{ij}}{}^{\mathrm{visc}} + q_{\mathrm{ij}}{}^{R}) \tag{34}$$

Equation of State
$$T_i = \frac{\partial \epsilon_i}{\partial s_i} \; where \; s_i = s_i(\epsilon_i) \tag{35}$$

same as those introduced earlier. The conduction, viscous heating and heat fluctuation operators are introduced in Equations (36), (37), and (38). Some of the variables are

Conduction (Equilibration)
$$q_{\mathrm{ij}}{}^{\mathrm{cond}} = K_{\mathrm{ij}}(\omega_{R^*}(|\vec{r}_{\mathrm{ij}}|))^2 \mathcal{F} \tag{36}$$

Conduction (Fluctuation)
$$q_{\mathrm{ij}}{}^{R} = \alpha_{\mathrm{ij}} \sqrt{k_B} \omega_{D^*}(|r_{\mathrm{ij}}|) \frac{\theta_{\mathrm{ij}}}{\sqrt{\mathrm{dt}}} \tag{37}$$

Viscous Heating
$$q_{\mathrm{ij}}{}^{\mathrm{visc}} = \frac{1}{2C_V}(\omega_R(|\vec{r}_{\mathrm{ij}}|))^2 [\gamma_{\mathrm{ij}}(\vec{e}_{\mathrm{ij}}.\vec{v}_{\mathrm{ij}})^2 - \frac{\sigma_{\mathrm{ij}}{}^2}{m}] - \sigma_{\mathrm{ij}} \omega_R(|\vec{r}_{\mathrm{ij}}|)(\vec{e}_{\mathrm{ij}}.\vec{v}_{\mathrm{ij}}) \xi_{\mathrm{ij}} \tag{38}$$

defined below.

K_{ij}: Similar to an inter-particle heat transfer coefficient. This is not quite right, however, given that it is internal energy which is being exchanged.

$\mathcal{F} = \frac{1}{T_i} - \frac{1}{T_j}$ is the *generalized force* or *affinity*. This is the driving force for internal energy exchange.

$\alpha_{ij} = (2K_{ij})^{1/2}$ A noise coefficient that controls the strength of the random heat fluctuations.

θ_{ij} : The time derivative of a brownian motion process with zero mean. The differential elements and white noise variables, θ, are anti-symmetric in contrast to ξ which has symmetry. The differential wiener elements also satisfy a slightly different Itō rule, $< dW_{ij}^{\epsilon} dW_{kl}^{\epsilon} >= (\delta_{ik}\delta_{jl} - \delta_{il}\delta_{jk})dt$. It should also be noted that θ & ξ are uncorrelated.

ω_{D^*}: This weight function is in principle different from its counter part ω_D. Note that $(\omega_{D^*})^{1/2} = \omega_{R^*}$.

The equations of motion can also be written in terms of differential Wiener elements following Espanol's original 1997 piece [8] where $dW_{ij}^{V} = \xi_{ij} dt$ and $dW_{ij}^{\epsilon} = \theta_{ij} dt$.

Momentum (Hydrodynamics)

$$d\vec{v}_i = \left[\sum_{j \neq i} \frac{F_{ij}^{C}(|\vec{r}_{ij}|)}{m} - \sum_{j \neq i} \gamma_{ij}\omega_D(|r_{ij}|)(\vec{e}_{ij}.\vec{v}_{ij})\vec{e}_{ij}\right]dt + \sum_{i \neq j} \sigma_{ij}\omega_R(|\vec{r}_{ij}|)\vec{e}_{ij} dW_{ij}^{V} \quad (39)$$

Internal Energy (Heat Transfer)

$$\begin{aligned} d\epsilon_i = C_V dT_i = \frac{m}{2}[\sum_j [\omega_D(|\vec{r}_{ij}|)\gamma_{ij}(\vec{v}_{ij}.\vec{e}_{ij})^2 \\ - {\sigma_{ij}}^2(\omega_R(|\vec{r}_{ij}|))^2]dt \\ - \sum_j \sigma_{ij}\omega_R(|\vec{r}_{ij}|)(\vec{v}_{ij}.\vec{e}_{ij})dW_{ij}{}^V] \\ + \sum_j K_{ij}(\omega_{R^*}(|\vec{r}_{ij}|))^2(\frac{1}{T_i}-\frac{1}{T_j})dt \\ + \sum_j \alpha_{ij}\sqrt{k_B}\omega_{R^*}(|\vec{r}_{ij}|)dW_{ij}{}^{\epsilon} \end{aligned} \quad (40)$$

Once again an equivalent Fokker-Planck expression can be written which is equivalent to the previous equations of motion. This expression is shown in Equation (41). [8] where where $x = \{x_1, x_2, \dots x_N\}$ and $x_i = \{\vec{r}_i, \vec{v}_i, \epsilon_i\}$.

$$\frac{\partial \rho(x,t|x_o,t_o)}{\partial t} = [L^{VH}(L_{ij},\dots) + L^{HC} - L^{C}{}_{DPD}]\rho(x,t|x_o,t_o) \quad (41)$$

Where the viscous heating, heat conduction, and Liouvillian operators are defined in Equations (42), (43), (44), and (45).

Viscous Heating

$$L^{VH} = \frac{1}{2}\sum_i \sum_{j\neq i} \omega_D(|\vec{r}_{ij}|)L_{ij}(\gamma_{ij}(\vec{v}_{ij}.\vec{e}_{ij}) + \frac{L_{ij}{\sigma_{ij}}^2}{2}) \quad (42)$$

$$\text{where } L_{ij} = \vec{e}_{ij}.[\frac{\partial}{\partial \vec{p}_i} - \frac{\partial}{\partial \vec{p}_j} - \frac{1}{2}\vec{v}_{ij}[\frac{\partial}{\partial \epsilon_i} - \frac{\partial}{\partial \epsilon_j}]] \quad) \quad (43)$$

Heat Conduction

$$L^{HC} = \sum_i \sum_{j\neq i} \omega_{D^*}(|\vec{r}_{ij}|)\frac{\partial}{\partial \epsilon_i}[(\frac{\partial}{\partial \epsilon_j} - \frac{\partial}{\partial \epsilon_j}) - \mathcal{F}]K_{ij} \quad (44)$$

$$(\text{where } -\mathcal{F} = \frac{1}{T_i} - \frac{1}{T_j} \quad)$$

Liouvillian

$$L^{C}{}_{DPD} = \sum_i \vec{v}_i \frac{\partial}{\partial \vec{r}_i} - \sum_i \sum_{j\neq i} \vec{F}_{ij}{}^{C} \frac{\partial}{\partial \vec{p}_i} \quad (45)$$

Equation (46) serves as the equilibrium statistical weight expression.

$$\rho_{eq} = \frac{1}{Z} e^{\sum_i \frac{s(\epsilon_i)}{k_B}} \mathcal{P}(E_{tot}, \vec{P}) \quad (46)$$

The expression $e^{\sum_i \frac{s(\epsilon_i)}{k_B}}$ comes from the accessible microstates term in the statistical weight expression. The number of accessible microstates can be written as the density of

states multiplied by some "volume" of energy, $W_{\text{states}} = \bar{\Omega}(E)\text{dE}$. Rewriting Boltzmann's entropy formula, $s = k_B \ln(W_{\text{states}}) = k_B \ln(\bar{\Omega}(E)\text{dE})$, the term of interest, $\bar{\Omega}(E)\text{dE} = e^{s/k_B} = e^{\sum_i s(\epsilon_i)/\text{kb}}$, is obtained. Once again in order to achieve an equilibrium distribution ($\frac{\partial \rho}{\partial t} = 0$) each individual operator in the Fokker-Planck expression is set equal to zero and ρ_{eq} is assumed to take on the form of Equation (46).

$$L^{\text{VH}} \rho_{\text{eq}} = 0 \tag{47}$$

$$L^{\text{HC}} \rho_{\text{eq}} = 0 \tag{48}$$

$$L^{C}{}_{\text{DPD}}\, \rho_{\text{eq}} = 0 \tag{49}$$

(50) is sufficient for (47) to be the case. (51), (52), and (53) are sufficient for (48) to be

$$\gamma_{\text{ij}} = \frac{{\sigma_{\text{ij}}}^2}{4k_B} \left(\frac{1}{T_i} + \frac{1}{T_j}\right)^2 \tag{50}$$

$${\alpha_{\text{ij}}}^2 = 2K_{\text{ij}} \tag{51}$$

$$\left(\frac{\partial}{\partial \epsilon_i} - \frac{\partial}{\partial \epsilon_j}\right) K_{\text{ij}} = 0 \text{where } K_{\text{ij}} = K_{\text{ij}}(\epsilon_i + \epsilon_j) \tag{52}$$

$$(\omega_{R^*})^2 = \omega_{D^*} \tag{53}$$

The case. Given the above conditions it is the case that $\frac{\partial \rho(x,t|x_o,t_o)}{\partial t} = [L^{\text{VH}}(L_{ij}, \dots) + L^{\text{HC}} - L^{C}{}_{\text{DPD}}]\rho(x, t|x_o, t_o) = 0$ holds.

§ 5.2: Introduction to RNEMD, Thermal Conductivity

The determination of thermal conductivity through the method of RNEMD is similar to the determination of viscosity. In the case where it was desired to obtain viscosity the demon identified and swapped particles with the highest magnitude velocity component in a particular direction. When the goal is to obtain thermal conductivity the situation is slightly different. In this case the "demon" identifies particles with the highest or lowest

kinetic energy. The simulation domain is split into bins of a particular length. The Z = 0 and central bins are identified. The bin at Z = 0 will be the cold bin and the central bin will be the hot bin. The particle with the highest kinetic energy is identified in the cold bin and the particle with the lowest kinetic energy is identified in the hot bin. The velocities, $\vec{v_i} = v_{x,i}\hat{i} + v_{y,i}\hat{j} + v_{z,i}\hat{k}$, of these particles are then swapped. In this way a temperature gradient is imposed on the system. [15] The energy transferred in a single swap can be calculated as $\Delta \mathrm{E_s} = \frac{m}{2}(|\vec{v_i}|^2 - |\vec{v_j}|^2)$.In steady-state an equal magnitude of energy flows back through the system via thermal conduction the heat flux can be calculated as shown in Equation (54). As a result of this behavior a constant temperature gradient, $\frac{\partial T}{\partial Z}$, regime is established. Temperatures can be calculated across the simulation domain using the equipartition

$$< \mathrm{q} >= \frac{\sum_S \Delta \mathrm{E}_S}{2t \cdot A} \tag{54}$$

theorem. The equation for temperature is shown in Equation (55) where N is the number of particles in any given bin and i is the index for particles in the bin. The temperature gradient is obtained from linear regression on the temperature profile. Finally, Fourier's

$$T = \frac{2}{3\mathrm{N}\mathrm{k}_B} < \sum_{i=1}^{N} \frac{|p_i|^2}{2m} > \tag{55}$$

law of heat conduction, Equation (56), is used to obtain the value for thermal conductivity. [15]

$$q = -k\frac{\partial T}{\partial Z} \tag{56}$$

§ 5.3: Methodology - Thermal Conductivity Computation

The experimental set up for the determination of thermal conductivity is nearly identical to that for the simulations to determine viscosity. The isothermal DPD simulations were used as a starting point for this new set of simulations. The shear flow was first allowed to die out. Once the shear flow had died out particle velocities were assigned according to a Maxwell-Boltzmann distribution and the simulation was switched to DPDE. Applying RNEMD within the framework of DPDE the simulation was allowed to equilibrate such that a temperature gradient developed across the simulation domain. The velocities of particles in the hot and cold slab were swapped at a particular rate. The simulation domain is binned and temperatures are calculated for each of the bins following the procedure outlined in the § 4.2: Introduction - Reverse Non-Equilibrium Molecular Dynamics, Viscosity. The temperature gradient is then obtained via linear regression from the slope of the temperature profile. Heat flux is determined following the procedure outlined in the introductory section and thermal conductivity is determined via Fourier's Law. In one set of simulations the effect of α, a parameter which controls the strength of thermal fluctuations in internal energies is explored. In order to explore the effect of α its value is varied while holding the other parameters, including average temperature, constant. A temperature gradient is imposed unphysically using RNEMD. Multiple instances of these simulations are started with alpha values that vary between 10 and 50. An identical set up is used for exploring the effect of heat capacity. Finally, simulations starting at various temperatures along the phase envelope are performed with

a constant α and heat capacity value. These same simulations are performed at various values of B, the magnitude of the attractive portion of the cubic spline function potential.

§5.4: Experimental Results

The simulation box set up is identical to that for the previous set of RNEMD simulations. The swap of high and low kinetic energy particles occurs with a frequency of 20 exchanges every 1000 time steps. Swaps are made more frequently for high α values. Linear weighting functions are used for both of the weighting functions - ω_{R^*} and ω_R. For all simulations the noise coefficient is fixed at a value of 10. For the simulations at an average temperature of 1.0 with variation in the magnitude of heat fluctuations the heat capacity is set to 100 and the B-value is 1.0. The results are presented in Figure 23. The values of thermal conductivity are also presented

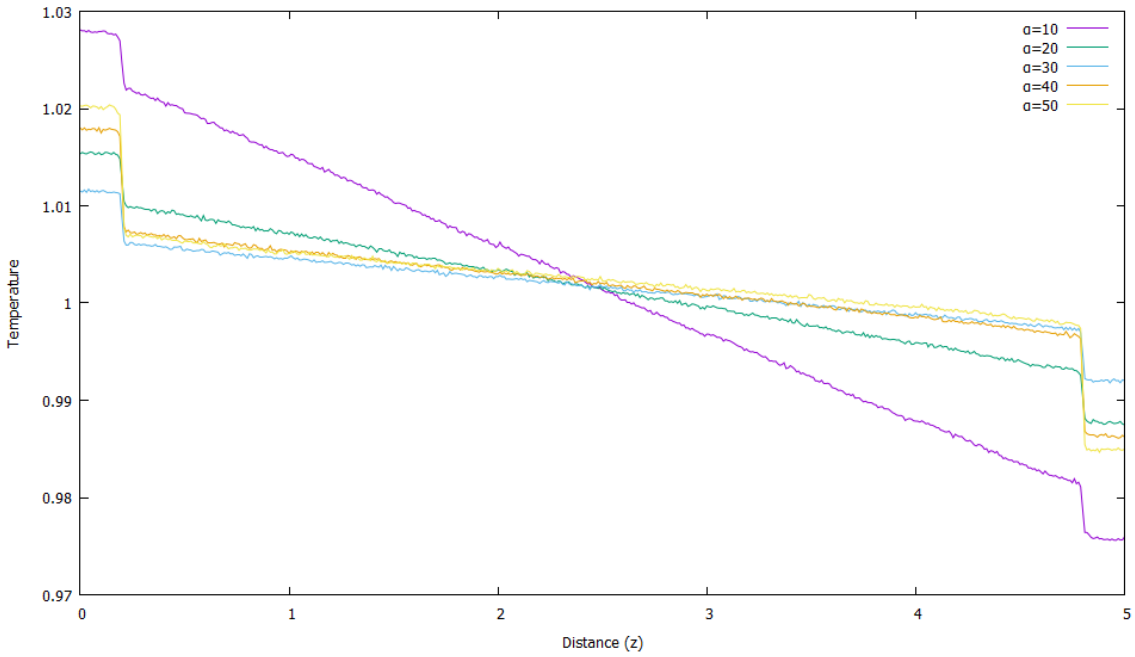

Figure 23: Temperature Profile, Varied Fluctuation Magnitude

In Table 5. For the simulations where heat capacity is varied the α value is fixed as 1.0. The temperature gradients are shown

Table 5: Thermal Conductivity vs Fluctuation Magnitude

α	Thermal Conductivity, k
10	551.39
20	1354.98
30	2563
40	2269.4
50	6919

in Figure 24 for variation in heat capacity. The values for thermal conductivity are shown in Table 6. The results for simulations at an attractive potential magnitude of B=1.0 for

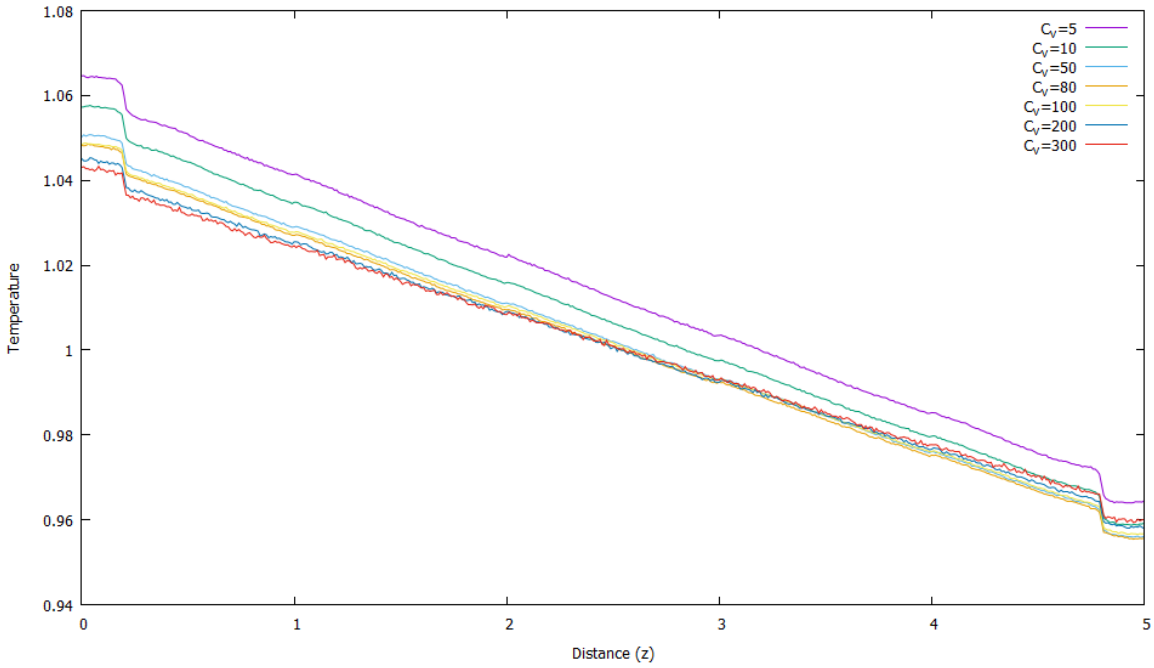

Figure 24: Temperature Profile, Variation in Heat Capcity

Table 6: Thermal Conductivity Vs. Heat Capacity

C_v	Thermal Conductivity, k
5	267.58
10	269.55
50	277.531
80	283.504
100	286.060
200	304.265
300	317.073

various temperatures are shown in Figure 25. Thermal conductivity values are shown in

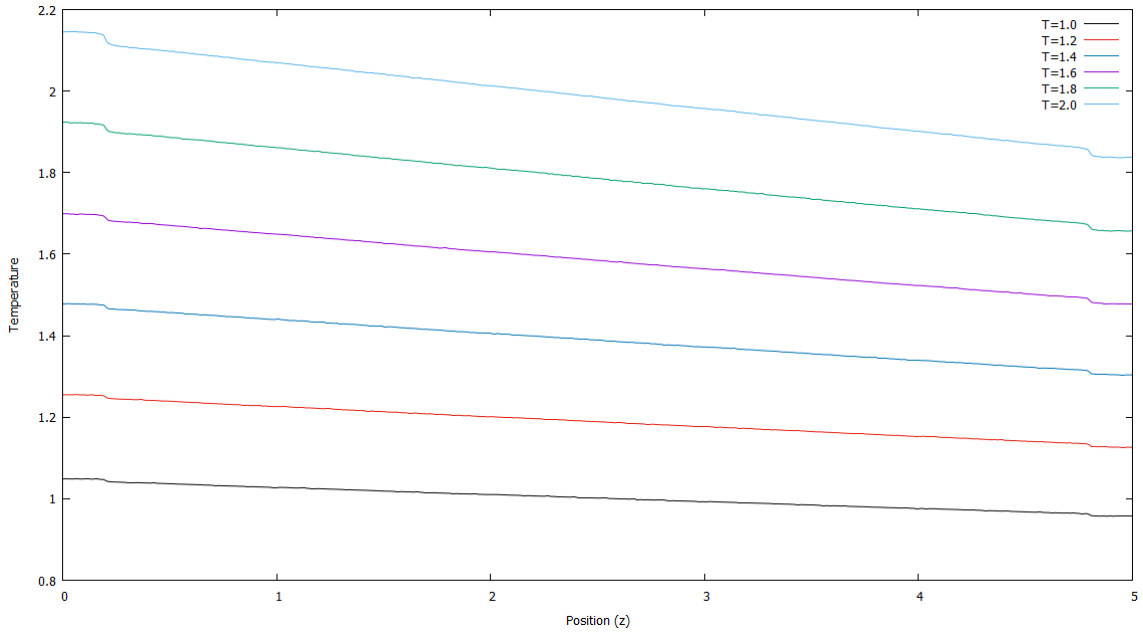

Figure 25: B=1.0, Temperature Profile

Table 7.

Table 7: B=1.0, Thermal Conductivity Values

Temperature	Thermal Conductivity, k
T=1.0	286.473

T=1.2	236.348
T=1.4	197.730
T=1.6	176.935
T=1.8	164.186
T=2.0	160.282

Future Directions

This work represents a first step in investigating a potential link between thermally driven hydrodynamic instability due to the surface tension gradient and the self-organization of arrays of nanoparticles. The methodology and results developed over the course of this work will be applied to the larger project. The larger project includes using coarse-grained simulation to reproduce the Bénard cells which are characteristic of Bénard-Marangoni hydrodynamic instability and investigation of the significantly more complicated experimental system used in Egusa's experiments. Additionally, there is still much work to be done which falls within the scope of this work itself. There are still many RNEMD simulations along the phase envelope which remain underway or would benefit from the collection of further data points.

References

1. Abu-Nada, E. (2010). Modeling of Various Heat Transfer Problems Using Dissipative Particle Dynamics. *Numerical Heat Transfer, Part A: Applications, 58*(8), 660-679. doi:10.1080/10407782.2010.516681

2. Avalos, J. B., & Mackie, A. D. (1997). Dissipative particle dynamics with energy conservation. *Europhysics Letters (EPL) Europhys. Lett., 40*(2), 141-146. doi:10.1209/epl/i1997-00436-6

3. Avalos, J. B., & Mackie, A. D. (1999). Dynamic and transport properties of dissipative particle dynamics with energy conservation. *The Journal of Chemical Physics J. Chem. Phys., 111*(11), 5267. doi:10.1063/1.479780

4. Chaudhri, A., & Lukes, J. R. (2009). Multicomponent Energy Conserving Dissipative Particle Dynamics: A General Framework for Mesoscopic Heat Transfer Applications. *J. Heat Transfer Journal of Heat Transfer, 131*(3), 033108. doi:10.1115/1.3056602

5. Egusa, S. (2005). Synthesis, fabrication, and spectroscopy of nano-scale photonic noble metal materials. *PhD Thesis, University of Chicago*.

6. Egusa, S., Redmond, P. L., & Scherer, N. F. (2007). Thermally-Driven Nanoparticle Array Growth from Atomic Au Precursor Solutions. *J. Phys. Chem. C The Journal of Physical Chemistry C, 111*(49), 17993-17996. doi:10.1021/jp076720a

7. Español, P., & Warren, P. (1995). Statistical Mechanics of Dissipative Particle Dynamics. *Europhysics Letters (EPL) Europhys. Lett., 30*(4), 191-196. doi:10.1209/0295-5075/30/4/001

8. Español, P. (1997). Dissipative particle dynamics with energy conservation. *Europhysics Letters (EPL) Europhys. Lett., 40*(6), 631-636. doi:10.1209/epl/i1997-00515-8

9. Evans, L. C. (n.d.). *An introduction to stochastic differential equations*.

10. Frenkel, D., Smit, B., & Ratner, M. A. (1997). Understanding Molecular Simulation: From Algorithms to Applications. *Phys. Today Physics Today, 50*(7), 66. doi:10.1063/1.881812

11. Hoogerbrugge, P. J., & Koelman, J. M. (1992). Simulating Microscopic Hydrodynamic Phenomena with Dissipative Particle Dynamics. *Europhysics Letters (EPL) Europhys. Lett., 19*(3), 155-160. doi:10.1209/0295-5075/19/3/001

12. Kusaka, I., & Egusa, S. (2014). Size and Shape Control in Nanoparticle Formation by Hydrodynamic Instability.

13. Liu, M., Meakin, P., & Huang, H. (2006). Dissipative particle dynamics with attractive and repulsive particle-particle interactions. *Physics of Fluids Phys. Fluids, 18*(1), 017101. doi:10.1063/1.2163366

14. Mackie, A. D., Avalos, J. B., & Navas, V. (1999). Dissipative particle dynamics with energy conservation: Modelling of heat flow. *Phys. Chem. Chem. Phys. Physical Chemistry Chemical Physics, 1*(9), 2039-2049. doi:10.1039/a809502g

15. Müller-Plathe, F., & Bordat, P. (2004). Reverse Non-equilibrium Molecular Dynamics. *Novel Methods in Soft Matter Simulations Lecture Notes in Physics*, 310-326. doi:10.1007/978-3-540-39895-0_10

16. Panagiotopoulos, A. Z. (1995). Gibbs Ensemble Techniques. *Observation, Prediction and Simulation of Phase Transitions in Complex Fluids*, 463-501. doi:10.1007/978-94-011-0065-6_11

17. Satoh, A., & Majima, T. (2005). Comparison between theoretical values and simulation results of viscosity for the dissipative particle dynamics method. *Journal of Colloid and Interface Science, 283*(1), 251-266. doi:10.1016/j.jcis.2004.09.050

[i] Illustration inspired by Understanding Molecular Simulation
[ii] This section influenced by discussion with Dr, Kusaka
[iii] Most equations in this section from [1] with slight modifications.